Spacecraft observations of energetic neutral atoms

Master's Thesis
University of Turku
Dept. of Physics and Astronomy
Physics
2018
BSc. Anssi Ovaskainen
Examiners:
Prof. Rami Vainio
Dr. Heli Hietala

The originality of this thesis has been checked in accordance with the University of Turku quality assurance system using the Turnitin OriginalityCheck service.

UNIVERSITY OF TURKU
Department of Physics and Astronomy

OVASKAINEN, ANSSI: Spacecraft observations of energetic neutral atoms

Master's Thesis, 63 pages, 2 appendix pages
Physics
November 2018

The use of Energetic Neutral Atom (ENA) observations to remotely and globally survey populations of plasma in the context of space physics is examined. General characteristics of ENAs and the methods of their detection are covered, as well as three science cases that act as examples of the use of the technique. For sake of brevity, the coverage of the subject is mostly limited to detections of ENAs that have energies of 1 keV or more. The first three chapters are in the form of a literature review. The fourth chapter utilises previously published data to estimate ENA fluxes from the terrestrial ring current in Low Earth Orbit at energies exceeding 100 keV. This is done to examine the possibility of observing ENAs related to solar eruptions with a detector mounted to a micro-satellite.

The main advantage of ENA detections is their global nature. It would not have been possible to obtain the results shown in chapter 3 with more traditional *in situ*-observations of ions. ENA observations can be used to gain new insights into known systems and they open possibilities of discovering new phenomena. On the other hand, work is still under way to mitigate the technical limitations related to instrument sensitivity and available angular resolutions. While the observation technique is still under development, the concept has been proven to be sound many times over.

Keywords: Energetic neutral atoms, ENA imaging, Space instrumentation, Heliosphere, Ring current.

Contents

Foreword **1**

1 Energetic Neutral Atoms **2**

1.1 Typical collision targets for energetic ions in the heliosphere 3

1.2 Charge exchange collisions 4

1.3 ENA losses 5

1.4 Effects of gravity and radiation pressure 6

2 General description of instruments and data handling **8**

2.1 Some history 8

2.2 Background rejection 10

2.2.1 Before the aperture 10

2.2.2 At the aperture 12

2.2.3 At the detector 13

2.3 ENA energy measurement 13

2.4 ENA flight path measurement 14

2.5 ENA species determination 14

2.6 Data processing and reduction 15

2.6.1 Instrument calibration before launch 15

2.6.2 Computation of plasma characteristics from ENA data 16

2.6.3 Parametrised model 16

2.6.4 Constrained linear inversion 18

2.6.5 Computerised Tomography inversion 19

3 Observations with IBEX and TWINS **22**

3.1 IBEX 22

3.1.1 Auxiliary sensors of IBEX 24

3.1.2 Boundary between the heliosphere and interstellar space . . . 25
3.1.3 Notable results of IBEX observations 26
3.2 TWINS 29
3.2.1 Auxiliary Sensors of TWINS 31
3.2.2 Terrestrial ring current 31
3.2.3 Observations of a CIR-driven geomagnetic storm with TWINS 33

4 Terrestrial ring current as a foreground: Observations of solar ENAs from Low Earth Orbit 39

4.1 The motivation for looking for solar ENAs 39
4.2 Particle telescope 41
4.3 Estimation of solar ENA spectrum 41
4.4 Estimation of storm time ring current ENA spectrum 43
4.4.1 First estimation of spectrum 44
4.4.2 Iterative corrections to average energies 47
4.4.3 Spectrum estimation with iterated energies 48
4.4.4 Analysis based on a single hot pixel 50
4.5 ENA count estimation based on a single hot pixel 51
4.6 Estimations of signal to noise ratios 52
4.7 Comparison with an alternative spectrum of ring current ENA emission 55
4.8 Conclusions 56

5 Conclusion and outlook 58

Foreword

Energetic Neutral Atoms (ENA) can be used to image plasma populations remotely and globally. ENAs are the result of energetic ions capturing electrons from cold atoms via charge exchange collisions. The resulting ENAs, which in many cases retain the energies and propagation directions they had just before the collision, now have ballistic trajectories, which means that they can travel far away from the original plasma population.

The goal has been, on one hand, to build a general picture of the strengths and limitations of ENA observations. On the other hand, typical scientific results and possibilities of ENA observations are examined. Ultimately, this work is an introduction to its topic.

In the first chapter, the main characteristics of ENAs are covered, while the second chapter deals with the methods used to produce ENA detections and the processing of resulting data in a general sense. In chapter 3 two science cases are used to showcase the power of ENA observations, while in chapter 4 the feasibility of a CubeSat-mounted instrument meant to detect high energy ENAs with solar origins from low Earth orbit is examined. Finally, chapter 5 contains concluding remarks.

Chapters 1-3 are in the form of a literary review, while chapter 4 deals with ENA flux estimations based on previously published data. Since the research related to ENAs is constantly evolving, newer articles have been prioritised over older ones wherever practical. For sake of brevity, the main focus is on space instruments that detect ENAs with energies of 1 keV or more.

1 Energetic Neutral Atoms

Most of the gas in the heliosphere and outside planetary atmospheres is ionised. However, there are also populations of neutral atoms with low energies. When energetic protons or other ions collide with these, ENAs can be the result. After becoming neutral, these energetic particles are no longer affected by magnetic or electric fields and in many cases, the remaining effects of gravity and radiation pressure are also negligible. Also in many cases, the collision process doesn't introduce significant changes to the speed or direction of propagation of the energetic particle. This means that ENA detections can be used to conduct remote sensing of a plasma population. This task is difficult to accomplish with instruments that rely on intercepting ions since the motion of ions is bound by magnetic fields. An overview of the ENAs and their origins is necessary since these must always be kept in mind when data from ENA detectors is examined.

The characteristics of the ENA-producing collision mechanisms contribute to the way in which characteristics of a plasma population are mapped into a corresponding population of ENAs. Since the instruments discussed in this text are used to measure, among other things, ENA flux as some function of direction, it is useful to consider the different variables that affect this flux.

Flux for ENAs of a species i and energy E originating at a specific direction and an interval of distances represented by the vector $\boldsymbol{s}$ can be defined as

$$j_{ENA,i}(\boldsymbol{s}, E) = \int_s j_i(\boldsymbol{s}, E) \cdot \sum_k \left[\sigma_{ik}(E) n_k(\boldsymbol{s})\right] \cdot \exp\left[-D(\boldsymbol{s}, E)\right] \mathrm{d}s. \tag{1}$$

Here $j_i(\boldsymbol{s}, E)$ is the flux of energetic ions of species i and energy E, which are here assumed to have the same energies and momentary directions of propagation as the resulting ENAs. The index k refers to the neutral particle species from which the charge is removed, while the coefficient $\sigma_{ik}(E)$ is the charge exchange cross-section. The cross-section depends on the species of the particles taking part in the collision

as well as the energy of the ion. Coefficient $n_k(\boldsymbol{s})$ is the number density of cold atoms in the direction of $\boldsymbol{s}$, and the ENA optical depth $D(\boldsymbol{s}, E)$ corresponds to the loss of ENAs by ionising collisions. Finally, s is the distance from the site of collision to the receiving instrument. The integration is done over the interval of distances in direction of $\boldsymbol{s}$ where charge exchanges producing the detected ENA flux can occur. [1]

The aim of the rest of this chapter is to further examine the collision targets, collisions and optical depth included in Eq. (1). Also the effects of gravity and radiation pressure are briefly covered.

1.1 Typical collision targets for energetic ions in the heliosphere

The neutral particles with which the energetic ions collide can have their origins in local interstellar medium (LISM) or around planets and other macroscopic objects of the heliosphere [1]. The species, densities and energy spectra of these populations determine the likelihoods of different charge exchange reactions and thus they also modify the rates of ENA production and loss [2].

LISM neutrals are mostly H and He with small amounts of other elements up to Ni. Their chances of getting ionised become larger as they get closer to the Sun. Ionised LISM-originating particles then form a population of the so-called pick-up ions. These migrate, as a component of the solar wind, back to the edges of the heliosphere, where they have a chance of becoming neutral again through charge exchange collisions [3]. This background of LISM-originating neutrals is especially useful as a source for ENAs that retain information about the solar wind. Also the interaction region between LISM and heliosphere, and the LISM itself can be studied, as is seen in chapter 3.

Cold neutral particle populations around planets consist of upper regions of

atmospheres and matter separated from the planets and their moons. For example, ions trapped by the terrestrial magnetic field can undergo several charge exchanges with Earth's atmosphere's upper regions, which results in Low Altitude Emission (LAE) of ENAs from auroral regions [4]. On the other hand, Saturn's magnetosphere has a population of atomic nitrogen, which is outgassed from its moon Titan [5]. The Sun-facing side of Mercury's magnetosphere is pressed below the planet's surface, which allows the solar wind to break neutral atoms free from Mercury's crust [6]. Similar sputtering can also happen when the solar wind meets smaller bodies, like asteroids and grains of dust [1].

The electron-giving collision targets need not always be neutrals. For example, in the solar corona protons can charge-exchange with partially ionised O, Si or Fe during a flare event, which produces ENAs of very high energies [7]. This case is examined further in chapter 4.

1.2 Charge exchange collisions

The most common ENA producing collision is one where an energetic ion collides with a colder neutral or ion and in the process steals an electron, thus becoming neutral and leaving a cold ion behind. Since protons and hydrogen are ubiquitous in space, the reaction usually examined in literature is the resonant case of

$$\mathrm{H} + \mathrm{H}^+ \rightarrow \mathrm{H}^+ + \mathrm{H}. \tag{2}$$

The word "resonant" refers to the fact that the colliding ion and target atom have similar ionisation potentials, and thus reaction (2) can happen without any change in the total internal energy of the system. On the other hand, reaction

$$\mathrm{He} + \mathrm{H}^+ \rightarrow \mathrm{He}^+ + \mathrm{H}. \tag{3}$$

is not resonant, and there is a total internal energy difference between the left and

right sides of this reaction. This additional energy is brought in by the energetic ion, which results in the cut-off seen in Fig. 1 between 0.1 and 1 keV. The cut-offs near 1000 keV are caused by energetic particles having very high speeds and thus they spend very short times close enough to the collision targets [8]. This results in a smaller probability of charge exchange. This introduces a natural upper limit to the energies that the ions studied by ENA observation can have.

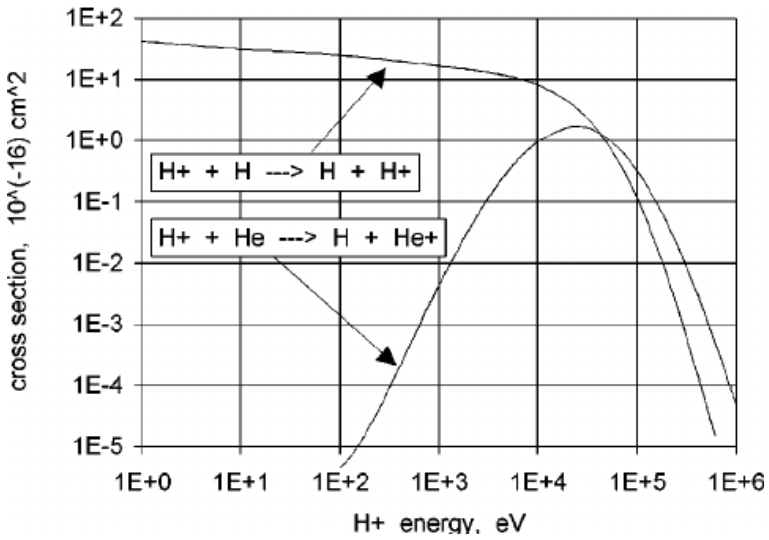

Figure 1: Charge exchange collision cross sections for two processes as functions of collider energy. Image taken from [1].

In the case of resonant collisions, the assumption that the momentum and direction of propagation for the more energetic particle are conserved is usually valid. This is not the case with non-resonant collisions, where the change of energy can manifest itself as a change of momentum. [8]

1.3 ENA losses

The main mechanisms of ENA loss are photoionisation by solar radiation and collisions with particles. The variable D of equation (1) can be defined [1] as

$$D = \int \beta \mathrm{d}t. \tag{4}$$

Here the integration is over the flight time of the ENA, while β is the ENA loss rate [9]. The loss rate can be defined as the sum

$$\beta = \beta_{cx} + \beta_{ph} + \beta_{el}. \tag{5}$$

Here β_{cx} refers to losses from further charge exchange collisions, β_{ph} to losses from photoionisation and β_{el} to losses by impacts with free electrons. One more loss mechanism is collisions with macroscopic bodies. This causes shading of flux for example in extended magnetospheres of gas giants that enclose moons and dust [10].

If enough information about the distributions of loss-related particles and relevant collision cross sections is available, an alternative definition for the ENA optical depth is of the form

$$D(\boldsymbol{s}, E) = \int_s \sum_m \left[\sigma_{im}(E) \cdot n_m(\boldsymbol{s})\right] \mathrm{d}s. \tag{6}$$

Here index m refers to the species of loss-producing particle. [10]

1.4 Effects of gravity and radiation pressure

While lensing by gravitation is less significant when studying the neutral solar wind or observing the ring current of Earth's magnetosphere from Earth's orbit, it does pose a potential source of error in case of longer propagation distances, for example when ENAs detected at 1 AU originate close to the heliopause [11]. The equation of motion for a hydrogen ENA in the heliosphere can be written as

$$\frac{\mathrm{d}^2\boldsymbol{r}}{\mathrm{d}t^2} = \frac{-GM\left[1 - \mu\left(v_r(\boldsymbol{r}), I_{tot}(t, \phi, \lambda)\right)\right]\boldsymbol{r}}{|\boldsymbol{r}|^3}. \tag{7}$$

Here $\boldsymbol{r}$ is the distance vector from the Sun, G is the gravitational constant, and M the solar mass. Equation (7) is an equation of motion for a particle in a spherical gravitation well modified with the variable μ. The value of μ is the ratio of the forces

caused by radiation pressure and gravitation. This ratio depends on the species and radial velocity $v_r(\boldsymbol{r})$ of the particle, as well as the integrated solar Lyman-α flux $I_{tot}(t, \phi, \lambda)$. The flux I_{tot} depends on time t, solar latitude ϕ and solar longitude λ. [12]

The magnitude of the radiation pressure depends on the species of the affected atom since the radiation pressure effect can only manifest itself if the solar radiation met by the atom has a frequency close to the resonance frequency of the atom. The resonance considered here relates to atom excitation and subsequent emission of a photon. In the case of H the resonance frequency corresponds with the frequency of the Lyman-α radiation, and thus we can have situations where the force of radiation pressure equals the force of gravity. On the other hand, noble gases like He are unaffected by radiation pressure, while lighter metals like Li, Na and Mg can experience significant acceleration. [13]

In addition to Sun also planets and moons can act as notable gravitational lenses if the ENA flies into the sphere of influence of such a body [14]. Usually, the resulting deflections of trajectory are insignificantly small or cause an error smaller than the angular resolution of the used instrument. They can also be countered by discounting those ENA detections that have possibly resulted from detecting particles that have made close bypasses of massive bodies. However, if the trajectory of the ENA must be reconstructed precisely over distances of the same magnitude as the radius of the heliosphere, modeling the effects of gravity becomes necessary [11].

2 General description of instruments and data handling

A typical instrument designed to detect ENAs is a particle telescope with the ability to filter out charged particles and photons, which have similar energies as the observed ENAs. This is necessary because the detectors used for measurement of particle impact and/or energy cannot distinguish photons, charged particles and neutrals from each other.

The subtype of instrument chosen for a given task is determined by the kinetic energy range of the ENAs to be observed. Also, the characteristics of the unwanted particle and radiation background met by the instrument on its orbit play a role in the selection and design process. The energy ranges of instruments can be tentatively divided as ultra-low energy (less than 0.5 keV), low energy (0.1-50 keV) and high energy (over 10 keV) [1]. In this work, for the sake of brevity the discussion of instruments and scientific accomplishments is limited to detectors designed for low and high energies. This is not to imply that the ultra-low energy range would be somehow less useful. For example, the < 1 keV neutral atoms surrounding Mercury [6] and Moon [15] are under active study.

First, the history of ENA instrumentation is given in brief. After this, subsections are organised according to the different functions an ENA instrument may perform in order to yield meaningful data. Finally different methods of computing ion fluxes from ENA fluxes, i.e., inverting functions similar to Eq. (1), are briefly covered.

2.1 Some history

First dedicated ENA detectors were flown already on the sounding rockets of the 1960s. Because of technical difficulties mostly related to background rejection and low ENA fluxes and throughput, first succesfull dedicated spacecraft-mounted ENA

instruments were not flown before the 1990s. [1]

The detectors designed for observation of energetic charged particles could sometimes detect ENAs serendipitously. In these cases, the true nature of the detected particle had to be inferred from previous knowledge or simultaneous and independent measurements. For example, the Voyager 1 spacecraft carried an instrument called LECP (Low Energy Charged Particle) that was designed for detection of energetic ions and X-rays. In [16] an observation of elevated levels of radiation emanating from the upstream of the bow shock of Saturn's magnetosphere is shown to have been most likely caused by ENAs. In that case, it was possible to discount ions, electrons and photons as sources of the registered counts because there were no known processes that would have motivated such assumptions. Detections like these were able to showcase the usefulness of ENA observation and they were part of the reason why the building of dedicated detectors was finally approved and funded.

Dedicated and successful low and high energy ENA instruments are listed in Table 1. Most of the text in this chapter is based on examination of similarities and differences between PIPPI-SSD, INCA, HENA, MENA, TWINS and IBEX-Hi. Because of this, the content of sub-chapters 2.2-2.5 is based on the corresponding articles mentioned in the rightmost column of Table 1. Figure 2 features images of PIPPI-SSD, MENA and HENA, while images and further descriptions of IBEX and TWINS are included in chapter 3.

Table 1: Dedicated and successful ENA instruments of higher energy ranges arranged in chronological order of the time of the start of observations. The "Reference"-column contains articles that describe the instruments.

Instrument	Spacecraft	Operating time	Energies [keV/nucl.]	Main object of study	Reference
PIPPI-SSD	ASTRID	01/95-02/95 [17]	13-140	Earth's magnetosphere	[18]
INCA	Cassini	08/99-2017 [19]	10-50	Saturn's magnetosphere	[20]
HENA	IMAGE	03/00-12/05 [21]	10-500	Earth's magnetosphere	[22]
MENA	IMAGE	03/00-12/05 [21]	1-30	Earth's magnetosphere	[23]
NUADU	TC-2	09/04-	45-158	Earth's magnetosphere	[24]
TWINS	USA-184, USA-200 [25]	06/08-	1-100	Earth's magnetosphere	[26]
IBEX-Hi	IBEX	12/08- [27]	0.5-6	Heliosphere	[28]

2.2 Background rejection

For an ENA instrument, the typical unwanted background consists of charged particles and photons, which have energies similar to or higher than the ENAs that the instrument was built to detect. The flux of this background is often much higher than the corresponding ENA flux. In addition, ENA instruments aren't immune to internally produced false detections or penetrations by very high energy particles. The causes of error coming from outside are mostly handled before or at the aperture, while the internal causes are accounted for at the detector.

2.2.1 Before the aperture

The typical way of dealing with charged particles is to install charged elements in front of the aperture, which provide electrostatic deflection. Here optimisation of design consists primarily of minimising the negative impact on the geometric factor of the instrument while ensuring that charged particles from a wide enough range of energies are deflected. These charged elements pose an upper limit to the energy of the ENAs that can be distinguished from charged particles with good confidence. The minimum energy that a charged particle must have in order to avoid deflection is also the maximum energy limit for observable ENAs. Ideally, the flux of particles with energies above this maximum is very small when compared with the ENA flux at the highest energy channel in use.

For instruments mentioned in Table 1, with the exception of IBEX-Hi, electric potential differences across the aperture are formed between plates, which are parallel to the paths of detectable ENAs. The material of these plates can be for example magnesium or stainless steel. To inhibit reflections of photons and particles from the plates, serrations machined into the plates or, in the case of MENA, coating with dendritic cupric oxide could be used [23]. It was noted in [26] that for two devices of similar design, the serrations provided superior results.

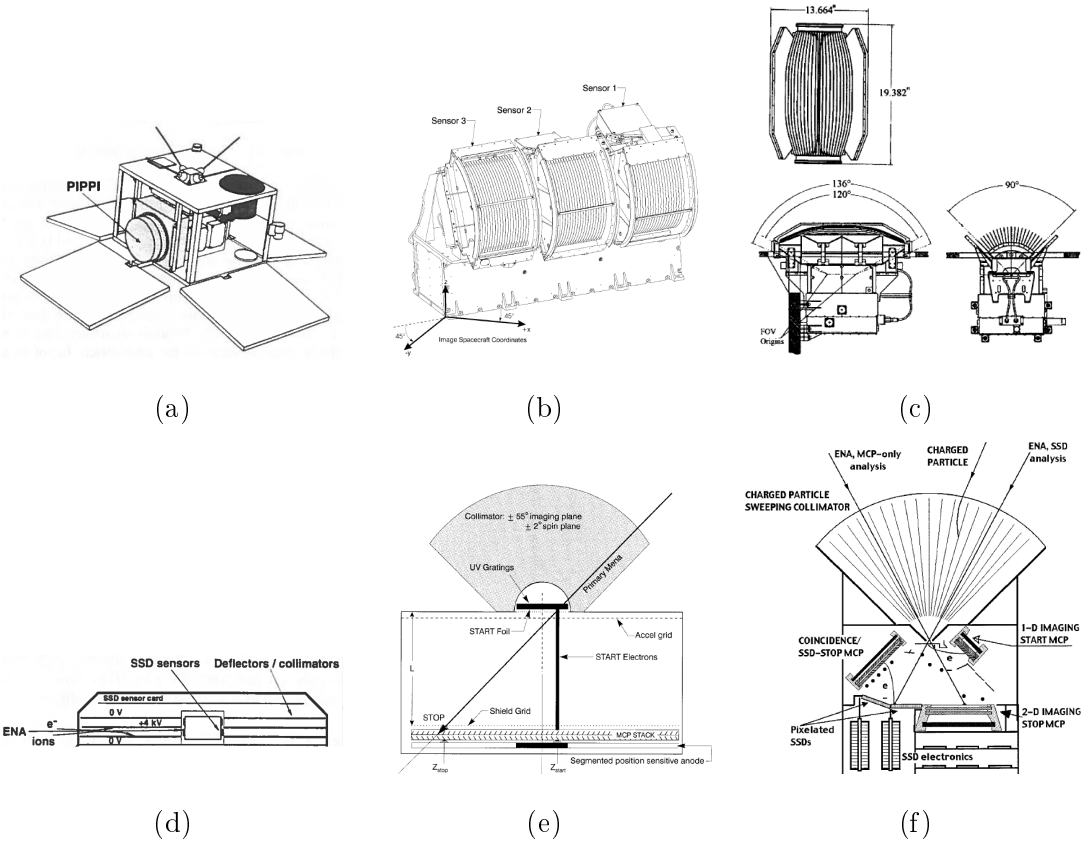

Figure 2: Some of the instruments shown in table 1: (a) ASTRID-microsatellite with PIPPI-instrument, (b) IMAGE MENA with its three identical instruments installed at different angles to eliminate blind spots, (c) IMAGE HENA, which was a modification of INCA, (d) cutout of PIPPI-SSD, (e) cut-out of MENA, (f) cut-out of HENA. Images (a) and (d) taken from [18], images (b) and (e) from [23] and (c) and (f) from [22].

The aperture of IBEX-Hi is annular, and a different solution is used. The collimator is designed to restrict the passage of particles coming from outside the instrument's field of view (FoV), and it is biased to + 10 kV to deflect ions away from the aperture. Electrons are deflected by two concentric circular rails installed above the annular collimator assembly and biased to -3.1 kV. Particles reflecting from the elements surrounding the aperture were determined to be stopped by the collimator in most cases. [28]

While it might seem reasonable to use magnets to deflect charged particles, this is not done in the instruments shown on Table 1. The only mention of magnetic deflection in the sources listed in Table 1 could be found in [18], where it was concluded that the use of "broom magnets" at the entrance of the aperture actually increased the flux of unwanted particles to the detector. The use of magnets in PIPPI was not researched further. Magnetic deflection has been used in charged particle detectors and detectors capable of measuring ENAs, but in many cases, it may be easier to use purely electrostatic deflection [1].

2.2.2 At the aperture

The aperture and the assemblies associated with it are responsible for blocking out photons. The background of UV radiation is commonly handled by installing a foil or a grating to the aperture.

Foils in ENA detectors can be designed to meet multiple objectives. The foil can be used to produce secondary electrons, which are used to determine the starting time of a detection. If no attenuating grating is present the foils must be thick enough that they attenuate UV flux by themselves. If the detector relies on the electrostatic collimation of particles that have passed the entrance aperture, the foil at the entrance may also be used to ionise ENAs prior to their introduction to the collimator. Ionisation by collision with a surface, resulting in the ion scattering away

from that surface, has been used in instruments designed for energies of 1 keV or less.

Gold gratings have been used to attenuate UV radiation in IMAGE MENA and TWINS [23, 26]. The gratings have been designed so that the period of gaps is almost twice the wavelength of the main background of Ly-α (121.6 nm) radiation. The gaps themselves are a fraction of this wavelength, 60 nm for MENA [23] and 45 for TWINS [26]. In these two instruments, the secondary electron producing 5 nm thick carbon foil is attached below the gratings, to the same grid onto which the gratings are attached.

2.2.3 At the detector

The main method of discarding false readings caused by cosmic ray penetration and associated secondary particles is by detection logic. If the ENA must pass through several surfaces after entering the aperture, these surfaces feature a way to record the passing, and these records along with their timestamps can be used to isolate only those detections where all of the surfaces have been penetrated in the correct order, with reasonable time gaps between the penetrations. Examples of this can be seen in [28] and [20].

Electrostatic deflection can also be used to redirect unwanted secondary particles inside the detector. For example in TWINS the Micro Channel Plate (MCP) installed above the stop-signal producing 1D position sensor has its upper surface biased to the voltage of -12 V [26].

2.3 ENA energy measurement

Solid State Detectors (SSD) used in higher energy ENA detectors are intrinsically suited for measurement of the energy of the impacting particle since the magnitude of the change of current through a pixel depends on this energy. With MCPs only

the location of the impact can be determined, which means that time of flight (TOF) measurement, possibly with species determination, must be used in order to calculate the kinetic energy of the ENA. In IBEX-Hi electrostatic deflection of ionised ENAs inside the instrument is used to set passbands of energy, which are periodically altered between six possible settings [28].

2.4 ENA flight path measurement

The apertures of the instruments are designed to constrict the angles from which ENAs can arrive. This way, even observations with single-pixel detectors such as those in IBEX can be matched with specific areas of the sky. Besides this, 1D and 2D slit cameras are used.

In a 1D slit camera like the one depicted in panels (b) and (e) of Fig. 2 one coordinate is determined by the heading the detector is facing, while the other is determined by the angle at which the particle travels between the electrostatic baffles. The detector at the bottom of the camera only measures impact distance from the area that is directly under the aperture slit. Because of this, spacecraft spin or a turning instrument platform must be used to produce 2D maps of the sky. The area of the slit that the particle penetrates is not included in the recording of data. On the other hand, in 2D slit cameras like the one depicted in panels (c) and (f) of Fig. 2 the detector at the bottom has the ability to record 2D data about the impact location.

2.5 ENA species determination

Time of flight data gathered from foil penetrations together with energy measurements with SSDs can be used to determine the mass of the particle. This type of mass estimation can be supplemented by measuring the number of secondary electrons emitted in foil penetration since this can be dependent on the mass of the

penetrator. By itself, the secondary electron amount is not accurate enough for anything else except a statistical determination of the ratios of different species of ENAs during some time interval [26].

2.6 Data processing and reduction

As can be seen from the previous subsection, valid ENA detections by dedicated instruments can be binned by direction of propagation and energy. In addition, particle species can often be at least estimated. Because of this, the cleaned up data from instruments is typically presentable as sky maps or spectra corresponding to specific energy intervals and particle species.

Because of the technical characteristics discussed above, the ENAs detected by the instrument are only a fraction of the ENAs propagating towards the instrument within its field of view. Together with detector inaccuracies, this means that determining the response of the instrument by pre-flight calibration or in-flight tests is necessary. This then allows the data to be used in further analysis, which leads to results that are comparable with those achieved by other means and can be refined into estimations of the characteristics of the source ion population.

2.6.1 Instrument calibration before launch

The instrument responses to known fluxes and propagation angles of energetic particles and sources of background radiation are tested before launch. This is necessary in order to calculate the per pixel and/or total responses of the instrument, which can be used to constrain the geometric factor of the instrument [22]. On the other hand, inversion from ENA flux to ion flux is done for each pixel individually, which also requires information about instrument response [29, 30].

The calibration is also used to determine and anticipate inaccuracies in measured quantities. As a result, a model of the instrument can be constructed, which can

then be used to anticipate possible results of observing a source with specific characteristics. If several instruments with different vantage points are used to observe the same phenomenon simultaneously, cross-calibration of these instruments provides higher consistency of results [26].

2.6.2 Computation of plasma characteristics from ENA data

The inversion of ENA flux into ion flux is non-trivial and requires, besides detailed knowledge of the instrument response, prior knowledge or modelling of the source particle populations situated within the instrument's field of view. Verification of inversion results can be done by comparing them to suitable independently obtained data from plasma instruments or other ENA instruments. The methods of inversion can be verified and refined by applying them to realistic test problems.

After the calibration results have been used to compensate for instrument-related errors, the ENA data can be used in further analysis. Three methods are briefly covered in following subsections, based on the following sources: Parametrised model [31], constrained linear inversion [29] and computerised tomography [30].

While the above three methods are used to produce static images, ENA fluxes can also be used to refine simulations, which aim at determining the way in which the ion distributions change in time. The algorithm by which the ENA data is assimilated must be carefully chosen to account for the instrument errors and high dimensionality of the ENA data [32].

2.6.3 Parametrised model

In the parametrised model, counts received by pixel i are defined as

$$C_i = \int R_i \sigma \rho_n P_{3D} \mathrm{d}\zeta, \tag{8}$$

where R_i is the pixel-specific instrument response, σ is the relevant charge exchange

cross section, ρ_n is the density of neutrals, P_{3D} is the 3D ion pitch angle distribution and ζ represents the spatial coordinates, energy and time over which the integration is performed.

This method is developed for the case of a single detector producing a 2D image, and because of this, adiabatic invariance of the first kind (particle velocity perpendicular to magnetic flux density vector $\mathbf{B}$ depends only on $|\mathbf{B}|$) and energy conservation are assumed, and P_{3D} is replaced with an equatorial 2D pitch angle distribution P_{eq}. This is defined, for the purpose of using the chi-squared method, as a product of three basis functions multiplied by coefficients a:

$$P_{eq} = \sum_{i,j,l} a_{ijl} B_i(r) S_j(\phi_{MLT}) P_l(\theta_{pa}). \tag{9}$$

Here B is a standard B-spline, which depends on the radial coordinate r, S is a periodic B-spline, which depends on the azimuthal coordinate ϕ_{MLT}, and P is an even Legendre polynomial, which depends on the pitch angle θ_{pa}.

The degree to which the chosen expansion fits the data is denoted by

$$\chi^2 = \frac{1}{N_{pixels}} \sum_{\alpha=1}^{N_{pixels}} \left[\frac{d_\alpha - C_\alpha}{\sigma_\alpha} \right]^2. \tag{10}$$

where d_α is the observed number of counts and σ_α represents uncertainties of the measurement. The modelled total number of counts received by a pixel α can be written as a result of plugging (9) into (8):

$$C_\alpha = \sum_{ijl} a_{ijl} \int R_\alpha \sigma \rho_n B_i(r) S_j(\phi_{MLT}) P_l(\theta_{pa}) \mathrm{d}\zeta. \tag{11}$$

In order to constrain the solutions, it is required that the solutions be as smooth as possible. A relatively complex penalty term P_p, which depends on the second derivative of the solution, is used to achieve this. The equation to be solved to find values of a is the variation

$$\delta\left(\chi^2 - \lambda P_p\right) = 0, \tag{12}$$

where λ can be adjusted to vary the relative contribution of the smoothing. The results are values for coefficients a_{ijl}, which can be used to determine the equatorial pitch angle distribution [31]. An example of the results of such a convolution is shown in fig. 3 and at the end of chapter 3.2.3.

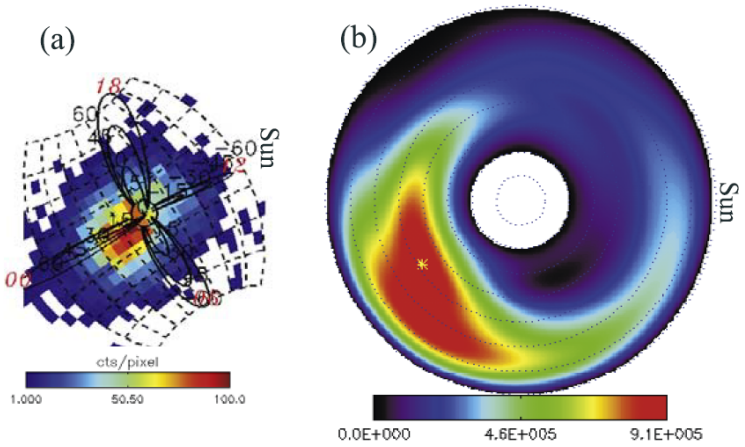

Figure 3: On the left counts obtained from IMAGE HENA and on the right a corresponding equatorial ion flux distribution obtained by integrating over pitch angles. Image taken from [33].

2.6.4 Constrained linear inversion

In constrained linear inversion the counts collected to pixel i are modelled as

$$C_i = \int\int K_i(L,\phi) J_{ion}^{eq}(L,\phi,\mu_{eq}) \mathrm{d}L\mathrm{d}\phi. \tag{13}$$

Here K_i contains information about pixel response, charge exchange cross section and density of neutrals, and J_{ion}^{eq} is the equatorial ion distribution. The coefficient μ_{eq} is the ion pitch angle cosine at the equator. Once again the locations are given in polar coordinates. Coordinate L is called the magnetic shell parameter. At the

geomagnetic equator the values of L correspond to distances from the center of the Earth in units of Earth radii. Coordinate ϕ is the magnetic longitude [34].

The difference between this method and that of the parametrised model is that now the quantity to be found is the ion distribution itself rather than coefficients of functions that describe the pitch angle distribution. Here, too the results are only 2D, corresponding to the estimated situation at the plane of the magnetic equator.

The count rate can be converted from an integral into a sum by binning it by the coordinates L and ϕ. This way, it can be written as the matrix

$$\mathbf{C} = \mathbf{K}\mathbf{J}. \tag{14}$$

As is mentioned in [35], the system of linear equations that can be solved for values of $\mathbf{J}$ can be written as

$$\mathbf{J} = \left(\mathbf{K}^T \sigma_{covariance}^{-2} \mathbf{K} + \gamma \mathbf{H}\right)^{-1} \mathbf{K}^T \sigma_{covariance}^{-2} \mathbf{C}. \tag{15}$$

In Eq. (15), $\sigma_{covariance}$ is used to account for inaccuracies and errors in measurements while the term $\gamma\mathbf{H}$ has a purpose similar to that of λP_p in Eq. (12): It is used to constrain the solution so that the result is as smooth as possible. The value of $\gamma\mathbf{H}$ can be determined iteratively by inversions of a simulated ENA image, which is based on a simulated ion distribution, which is estimated to be similar to the one resulting in the actual ENA counts. When the inversion result matches the simulated ion distribution, the parameter value can be judged to be correct [29]. An example of a result of using this method is seen in Fig. 4.

2.6.5 Computerised Tomography inversion

The Computerised Tomography inversion method can be used when ENAs are observed from at least two different vantage points, as in, for example, the original concept of TWINS [26]. As is seen in Fig. 5, this opens up the possibility of moving

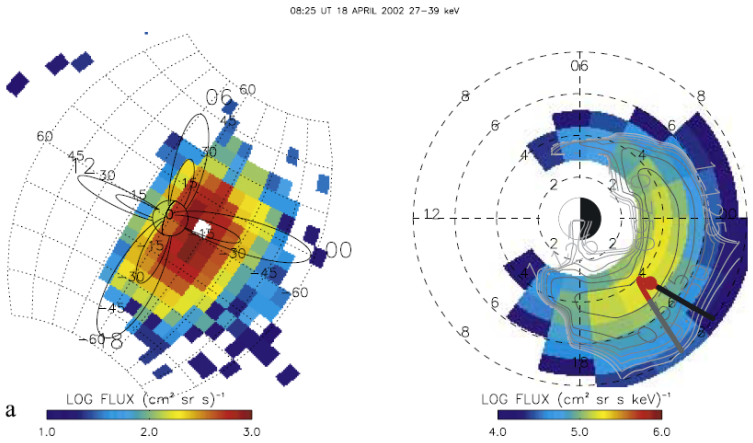

Figure 4: On the left ENA fluxes obtained from IMAGE HENA and on the right a corresponding ion flux distribution obtained by integrating over pitch angles. Image taken from [35].

from 2D maps to 3D distributions, provided that the spatial resolution of the ENA data is good enough. The number of counts received by pixel i is given by

$$C_i = \int\int\int\int A_i(\eta, \beta, E, t) J_{ENA} \sin\eta \mathrm{d}\eta \mathrm{d}\beta \mathrm{d}E \mathrm{d}t, \tag{16}$$

where A_i gives the instrument response and η and β are angular elevation and azimuth of the direction from which the ENA arrived. The J_{ENA} is defined as a line integral similar to Eq. (1). Contrary to the two previously presented methods, that integral is turned into a sum by dividing the ENA source space into discrete volumes, voxels:

$$(\mathbf{J}_{ENA})_M = (\mathbf{G})_{M\times N} (\mathbf{J}_{ion})_N \,. \tag{17}$$

Here index M refers to lines of sight and index N to voxels, while $\mathbf{G}$ contains information about the way in which the ion distribution in a voxel contributes to ENA flux in a specific line of sight. Solving this equation with a suitable algorithm allows voxel by voxel reconstruction of the parent ion distribution. When a 3D distribution is sought after, there should as many lines of sight per voxel as possible.

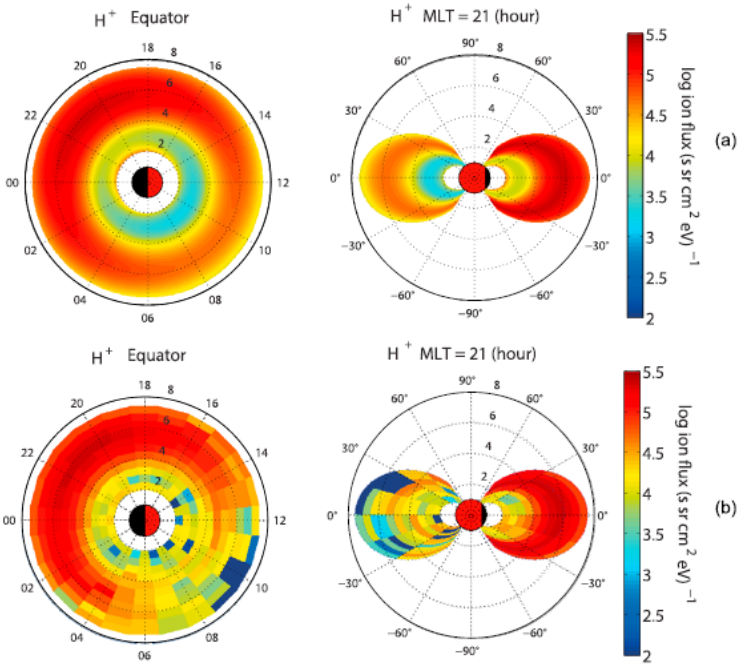

Figure 5: Top: simulated ion distribution seen from above the pole and from the plane of the magnetic equator. Bottom: Corresponding simulated ion distribution retrieved by applying the basic CT technique to simulated ENA images. Image taken from [30].

In other words, it is required that $M \geq N$. If this were not achieved, the problem would also be mathematically ill-posed.

3 Observations with IBEX and TWINS

This chapter is the first of the two showcasing practical applications of ENA observation. The two instruments considered in this chapter (IBEX, TWINS) and PATE in chapter 4 have been selected to offer different viewpoints to the use of ENAs, at different energy ranges. This chapter is in the form of literature review while chapter 4 consists of a new analysis, which is partially based on data from the IMAGE satellite.

3.1 IBEX

As can be seen from Table 1, IBEX (Interstellar Boundary EXplorer) is designed to detect ENAs at relatively low energies. Besides the IBEX-Hi sensor mentioned in chapter 2, it also has a lower energy ENA detector called IBEX-Lo, which has an energy range of 0.01 keV to 2 keV. As seen in Fig. 6, the sensors are broadly of the same type, the main differences being that in IBEX-Lo the ENAs are ionised by collision with a tetrahedral amorphous carbon surface and that IBEX-Lo can determine masses of particles based on TOF-measurements. While IBEX-Hi has Channel Electron Multipliers (CEM) as detectors, IBEX-Lo uses carbon foils to produce secondary electrons that generate "start"-signals as they hit an MCP, and the "stop"-signal is generated when the atom itself impacts the MCP [38].

The scientific goals of IBEX are to shed light on properties of the heliospheric termination shock and particle acceleration associated with it, solar wind properties in the heliotail and outside the termination shock, and the way in which LISM interacts with the heliosphere beyond the heliopause. These goals are potentially attainable with ENA detections since a large fraction of Local InterStellar Matter (LISM) is neutral, and charge exchange plays an important role in the interactions between solar wind particles and LISM. [38]

The apogee altitude of IBEX is approximately $52R_E$ (Earth radii) while its

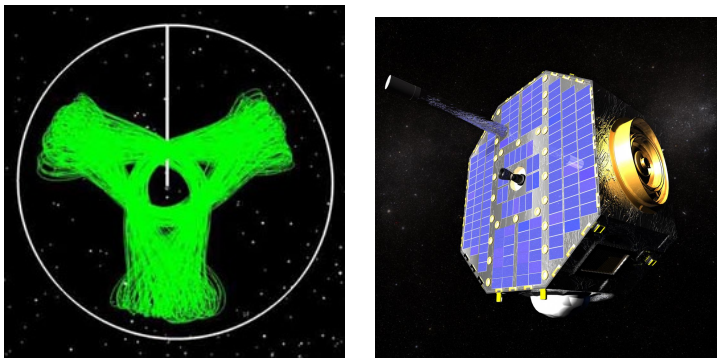

(a) (b)

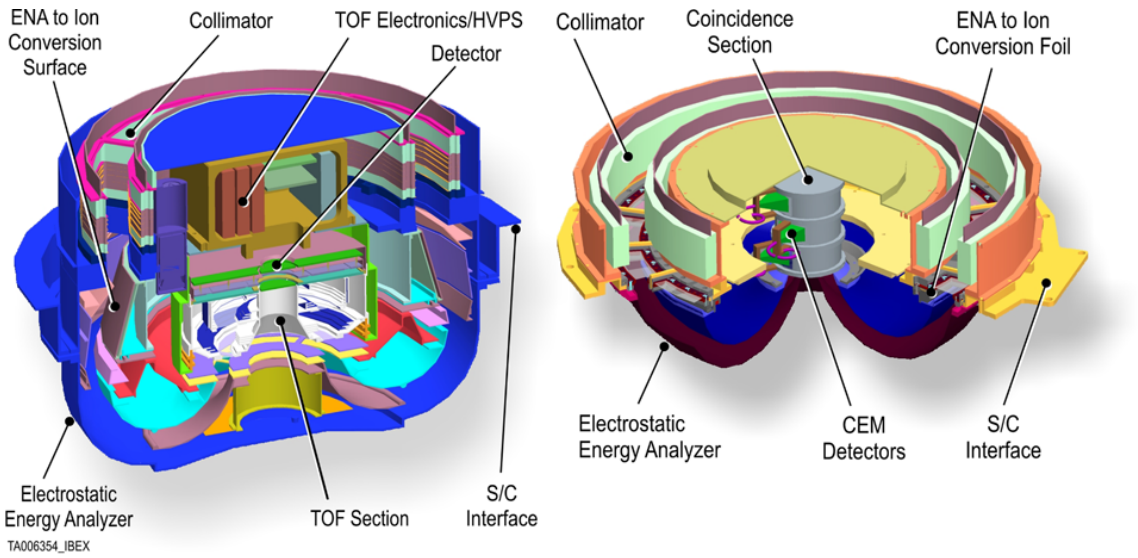

(c)

Figure 6: (a) The three-lobed orbit of IBEX with several orbital periods superimposed, with Earth in the center and orbit of the Moon in white, (b) IBEX spacecraft with the sun-facing solar panels and one of the two ENA instruments visible, (c) cut-outs of the IBEX-Lo and IBEX-Hi instruments. Image (a) is taken from [36], (b) is from [37] and (c) from [38].

perigee altitude is approximately $7R_E$ [39]. For the Moon, the corresponding values are $64R_E$ and $57R_E$. The orbit configuration shown in panel (a) of Fig. 6 was chosen to maintain the high apogee altitude while minimising the gravitational effect the Moon has on the orbit [36]. The high apogee is needed to maximise the time the spacecraft spends outside Earth's magnetosphere to avoid the particle background therein. When the spacecraft is below $10R_E$, ENA observations are paused and the time is spent, for example, on transfering data and correcting spacecraft pointing. The spacecraft has been designed so that the area covered with blue solar panels shown in panel (b) of Fig. 6 is kept pointing at the Sun. This maximises power production, shields the instruments mounted to the sides of the spacecraft from radiation and allows ENA instrument pointings to change gradually so that a full sky map can be created every six months [38].

3.1.1 Auxiliary sensors of IBEX

IBEX-Lo uses only 1/4th of its aperture when detecting oxygen. Its FoV is then $3.2° \times 3.2°$ instead of the full $6.5° \times 6.5°$ that is used for hydrogen and helium. Because of the smaller pixel size, a more accurate method of determining pixel locations in the sky was needed. Because of this, a star sensor was mounted coaxially with IBEX-Lo. [40]

Since the collimators of ENA detectors of IBEX can not reject charged particles with energies higher than 10 keV, the possibility of having a background of high energy particles had to be accounted for. This way, pixels with excessive background could be discarded from data. This was accomplished by installing the IBEX Background Monitor (IBaM) with a FoV of approximately 7° FWHM. The FoV of IBaM coincides with the FoV of IBEX-Hi. IBaM consists of a CEM with two carbon foils covering its aperture. The foils are used to reject particles with energies less than 14 keV and UV photons [41]. The charged particle count data from the IBaM can

be useful also when separated from the context of ENA measurements [42].

3.1.2 Boundary between the heliosphere and interstellar space

The structures comprising the boundary between the heliosphere and Local Inter-Stellar Medium (LISM) are shown in Fig. 7, together with the IBEX ribbon, an unexpected anisotropy in ENA flux discovered with IBEX in 2009 [27]. The termination shock is the boundary where the outward-moving solar wind becomes the heated and slowed plasma of the inner heliosheath. The inner heliosheath is situated between the termination shock and the heliopause. The heliopause is the boundary between plasmas and magnetic fields of solar and interstellar origin and the outer heliosheath outside the heliopause contains plasma that has been redirected by the solar magnetic field. The exact characteristics of the bow wave structure is still an open question [43].

Voyager probes crossed the heliospheric termination shock at a distance of roughly 90 AU [43]. Since the properties of the solar wind and LISM vary with time, the structures depicted in Fig. 7 are also variable. For example, the distance from the Sun to the heliopause may, according to a simulation, vary approximately 14 AU due to matter from solar eruptions temporarily enhancing the ram pressure of solar wind [44].

Besides ENA observations, outer parts of the heliosphere have also been observed *in situ* by Voyagers 1 and 2, of which the first one has already crossed the heliopause and the second is close to doing the same [45]. Additionally, scattering of solar Lyman-α radiation from H [46] and absorption of radiation from nearby stars at Ly-α wavelength [47] have been used to probe these outer regions.

While the interstellar charged particles get mostly deflected by the solar magnetic field, the neutrals can continue deep into the heliosphere, and be detected even at 1 AU. However, when inside they have a high chance of becoming pick-up

ions (PUI) via ionisation by charge exchanging with solar wind or collisions with UV photons. PUIs are then advected along the solar wind until they reach the heliospheric termination shock, where they may be deflected and/or charge exchange once again. Broadly, the ENA populations related to structures shown in Fig. 7 are either the neutral component of LISM or results of charge exchanges within the heliosheath. [43]

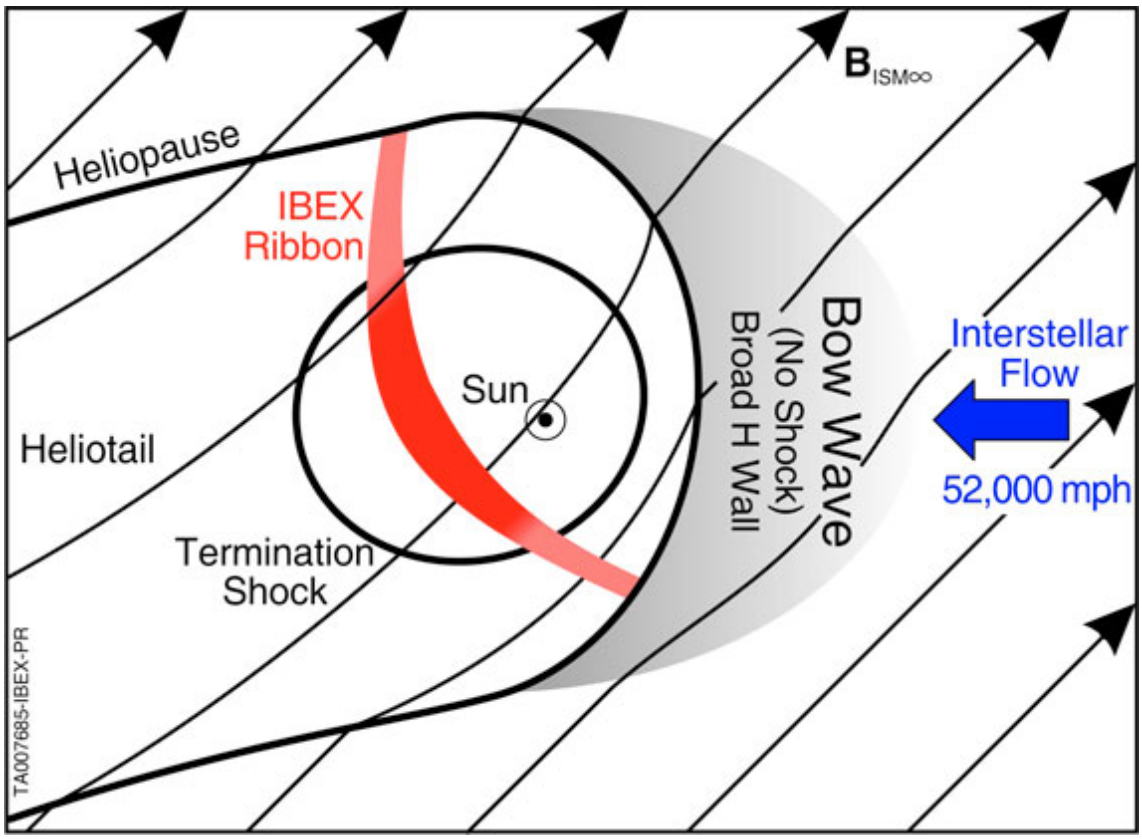

Figure 7: The heliosphere and its exterior from the point of view of IBEX observations. Image taken from [48].

3.1.3 Notable results of IBEX observations

The main data products of IBEX observations are maps of the whole sky made during periods of six months. Examples can be seen in Fig. 8, along with the effects of correcting for spacecraft motion around the Sun and ENA loss mechanisms within

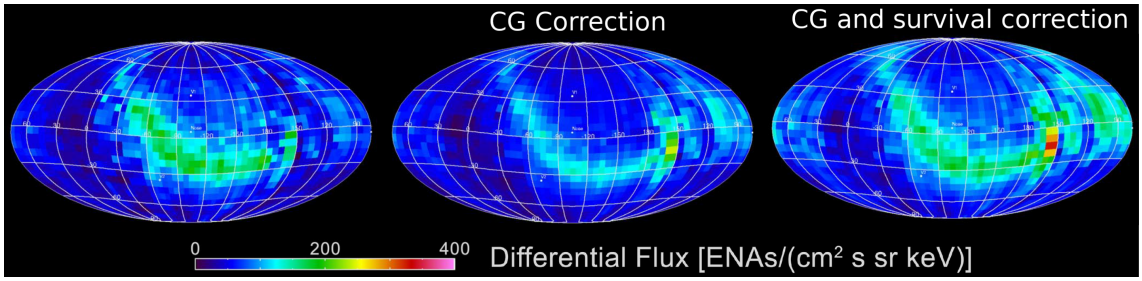

Figure 8: IBEX sky maps of differential ENA flux at energy 1.11 keV. At the center, corrections have been made for the Compton-Getting effect or biases due to the spacecraft motion around the Sun. On the right, CG-corrected fluxes have been extrapolated to 100 AU, in an attempt to remove the estimated effects of ENA loss mechanisms. The image on the left has neither of these adjustments applied. All three maps are from time period 26.12.2012-26.06.2013. Image adapted from [27].

the heliosphere. In each map of Fig. 8 the ram-direction or direction from which the LISM is flowing towards the solar system is in the middle of the map.

When the left and middle maps of Fig. 8 are compared, it is evident that in the ram-direction the fluxes are smaller after CG-correction, while the opposite is true for the edges of the maps, which show fluxes in the anti-ram direction. This is because the ENA fluxes at lower energies are higher, and in the ram-direction the ENA velocities in the spacecraft frame are sums of spacecraft and ENA velocities, resulting in higher observed kinetic energies. In other words, ENAs that should be binned to a lower energy channel, "leak" to a higher energy bin. The opposite is true in the anti-ram direction, where instead ENAs of the lower energy bin cannot be observed. Since the sums mentioned are those of vectors, the spacecraft motion also results in erroneous ENA propagation direction measurements for pixels not near the ram or anti-ram directions [49]. Essentially the Compton-Getting correction gives estimates of ENA fluxes as they would appear if the spacecraft were stationary with respect to the Sun. The maps seen here were made during the first half of the year, and an opposite bias can be seen for maps produced during the second half of the

year [27].

Comparison between the middle and right maps of Fig. 8 shows enhancement of flux in all directions. This is because the contributions ENA loss mechanisms and effects of radiation pressure mentioned in chapter 1 have been estimated for the given series of orbits and these estimates have been applied to estimate what the ENA fluxes would be at the distance of 100 AU. While in the figure the enhancement of fluxes seems isotropic, it must be noted that the survival probability does depend on ENA propagation direction and on solar activity during ENA flight time [49].

Figure 8 also features the IBEX ribbon. As is depicted in Fig. 7, the center of the ring-like anisotropy is in a direction parallel to the interstellar magnetic field, while in Fig. 8 the center of each map is the direction from which the neutral component of the LISM flows into the heliosphere. While the three maps depict ENAs at energy 1.11 keV, the anisotropy is visible in some form in all energy passbands of the IBEX ENA instruments [27]. Currently, there is no certainty of the cause of the ribbon. Most models as well as parallax measurements [11] position it somewhere within the heliosheath region [50].

Currently, the models that best explain the ribbon belong to the "secondary ENA"-category [27]. The formation of the ribbon emission according to these models happens as follows: First, ions of out-flowing solar wind charge exchange with the neutral component of the LISM within the heliosphere. The resulting population of ENAs can then cross the heliopause. Some of these ENAs are ionised by charge exchanges with LISM in the outer heliosheath, after which they are guided by the interstellar magnetic field. The ENAs coming to Earth from the direction of the ribbon are thought to originate in volumes where the interstellar magnetic field is perpendicular to the line of sight of detecting instruments. In this annular volume, the ions with pitch angles close to 90° may charge exchange with LISM so that the velocity vector of the resulting ENAs point towards the inner solar system [50].

The largest problem with these models is that the pitch angles of the ions gyrating in the interstellar magnetic field can become isotropic fairly quickly, possibly within days, while the corresponding mean time between charge exchanges in the heliosheath can be measured in years [51]. While secondary ENA models can explain the shape of the ribbon, its intensity is another matter.

Several mechanisms have been proposed to account for this issue. For example, magnetic mirroring caused by irregularities in the interstellar magnetic field may limit particle transport in the heliosheath, resulting in ions staying in the volume of ribbon origin long enough that a charge exchange becomes likely during their stay [52].

3.2 TWINS

TWINS (Two Wide-angle Imaging Neutral-atom Spectrometers) is a "mission of opportunity"-solution where scientific instruments producing publicly available data (accessible at [53]) were mounted to spacecraft that are so secret that the only image related to them can be seen in Fig. 9 (b). In this subfigure, the only spacecraft-related detail is the limits the spacecraft structure imposes on instrument FoV. Another constraint to the design of TWINS-instruments was that the spacecraft is kept pointing approximately towards the center of the Earth while being otherwise stabilised on all three axes of rotation. Since spacecraft rotation couldn't be used to augment instrument FoV, the ENA instruments and the associated Lyman alpha radiation detectors were installed on a turning platform. This platform takes 60 seconds to traverse 180°, which is the rotation needed for the instrument to scan its full FoV [26].

TWINS-1 was launched in June of 2006 while TWINS-2 was launched in March of 2008 [25]. TWINS-2 instrument suffered an unknown malfunction in the fall of 2016 [54], and last ENA data from this instrument is from 26/10/2016 [53]. After

this, TWINS-1 has continued to provide data from a single point of view. The main scientific goals of TWINS deal with establishing a global coverage of different processes in the magnetosphere, and the ways these processes relate to each other [26].

The orbits of the spacecraft can be seen in Fig. 9 (a), along with ions captured by the terrestrial magnetic field. While the Molnya-type orbits of the spacecraft may have been originally chosen for reconnaissance, they also work well for measurements of the ring current and other phenomena of the terrestrial magnetosphere. The orbits have apogees of 7.2 R_E, and approximate perigees of 0.2 R_E. The angular spacing of the orbits allowed the two spacecraft to have Magnetic Local Times (MLT) that could be several hours apart producing an opportunity to image same volumes of space from two vantage points at similar altitudes but on opposing sides of Earth. [25]

A cut-out of one of the four identical ENA detectors mounted on the two spacecraft is shown in Fig. 9 (c). This detector is a modified and improved version of IMAGE MENA: Energy range was increased from 1-30 keV/amu to 1-100 keV/amu and the method of minimising back-scatter from collimator plates was changed from Ebonol-C coating to more efficient serrations in the plates. The detector has a total FoV of 2.5 sr, an angular resolution of $4° \times 4°$, and a geometric factor of approximately 0.003-0.004 cm^2sr. [26]

A valid ENA detection proceeds as follows: First, after passing the collimator plates the ENA penetrates the "Start"-foil, creating a secondary electron, which is electrostatically guided into the electron anode in the middle. This anode is position sensitive, and it is used to determine the location where the ENA penetrated the foil. Second, the ENA hits the MCP and produces a detection at the position sensing ion anode, at which time the "Stop"-signal is produced. From these two detections of position and time, the ENA flight path can be reconstructed. [26]

3.2.1 Auxiliary Sensors of TWINS

To help with image inversions, each of the two instrument platforms includes two Lyman Alpha Detectors (LAD). These are used to detect solar Ly-α radiation scattering from the cold hydrogen geocorona, which provides the neutral targets for charge exchange collisions within the volume of magnetosphere studied with TWINS. Based on these data, the hydrogen density values needed for image inversions can be estimated. The $4° \times 4°$ FoVs of the detectors coincide with those of the ENA sensor heads. The detectors consist of a filter with a 10 nm passband to limit erroneous detections, and a CEM detector followed by electronics [55]. As in the case of IBaM, data from LAD can also be useful without the context of ENA image inversion [56].

The host spacecraft of TWINS were also equipped with TWINS Environmental Sensors to measure the immediate charged particle environment of the spacecraft. These contain dosimeters for energetic electrons and protons and top hat-type sensors to measure charging of spacecraft surfaces. [26]

3.2.2 Terrestrial ring current

Figure 10 portrays the terrestrial magnetosphere and the permanent electric currents associated with it. The magnetopause current forms as a result of gradient drift of charged particles. Neutral sheet current forms between magnetic fields of opposing directions and is part of the same current loop as the tail current. The field-aligned or Birkeland currents are divided into two categories: Birkeland-1 refers to currents that flow away from the ionosphere in the dusk side, while Birkeland-2 currents flow in the opposite direction. [58]

The terrestrial ring current exists as a movement of charged particles, which have been trapped by the magnetic field. In a magnetostatic case this current can be described as the diamagnetic current $\boldsymbol{j}$:

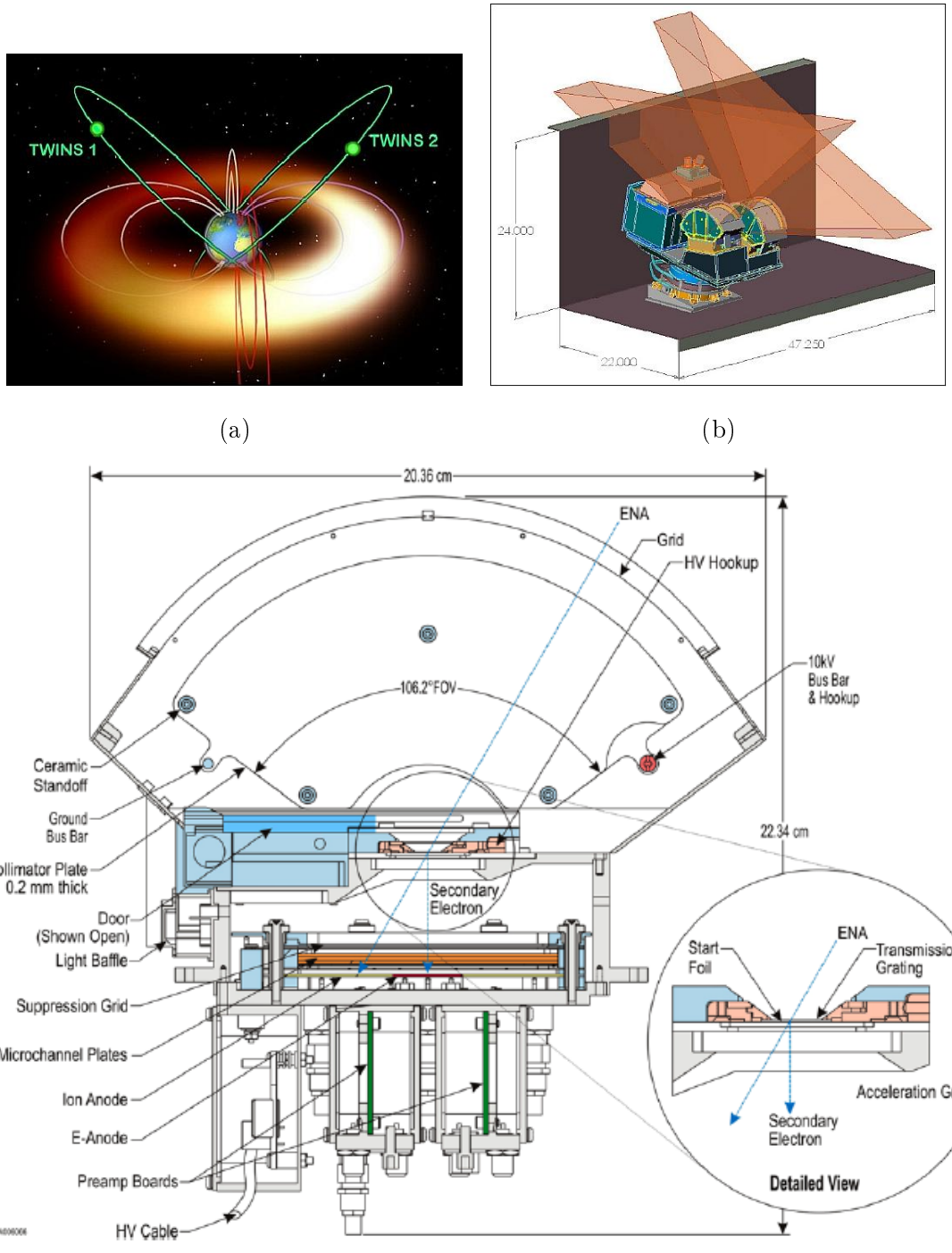

(a) (b)

(c)

Figure 9: Principle of TWINS: (a) orbits of the spacecraft together with the ring current, (b) installation of the two identical instruments, (c) cut-out of an instrument. Image (a) is taken from [57] and images (b) and (c) from [26].

$$\boldsymbol{j} = \frac{\boldsymbol{B}}{B^2} \times \left[\nabla P_\perp + \frac{P_\parallel - P_\perp}{B^2} \left(\boldsymbol{B} \cdot \nabla \right) \boldsymbol{B} \right]. \tag{18}$$

Here $\boldsymbol{B}$ is the magnetic flux density of the terrestrial magnetic field while $P_\perp$ and $P_\parallel$ are particle pressures perpendicular and parallel to $\boldsymbol{B}$. The terms on the right side in parenthesis correspond to the particle pressure gradient and curvature of the magnetic field [59]. From Eq. (18) it can be seen that the resulting current must be perpendicular to the magnetic field, the gradient of $P_\perp$ and radius of curvature of $\boldsymbol{B}$. In the case of the terrestrial magnetosphere, a current having the form of Eq. (18), when caused by movement of positive ions, flows from east to west.

The definition given by Eq. (18) ties together the ring current and the magnitude of the terrestrial magnetic field. If the shape of the magnetic field and particle pressure are kept constant and current is increased, B must decrease. Disturbance storm time (Dst) index describes the weakening of the horizontal magnetic field, which is mainly caused by changes in the ring current [60]. The values of this index are collected from ground stations near the equator. This weakening of the magnetic field can induce harmful electric currents in large terrestrial conductors like power grids and pipelines. On the other hand, increased particle fluxes around Earth can damage satellites [61]. Since geomagnetic storms have a significant impact on the workings of modern societies, the ring current and its evolution during storms are important objects of study, together with the rest of the phenomena within the terrestrial magnetosphere.

3.2.3 Observations of a CIR-driven geomagnetic storm with TWINS

The 22 July 2009 Co-rotating Interaction Region (CIR)-driven geomagnetic storm is used as an example of phenomena studied by observing ENAs from the ring current with TWINS. A CIR is formed when the fast solar wind from a coronal hole region of the Sun catches up to the slow solar wind. Usually, this happens at distances of

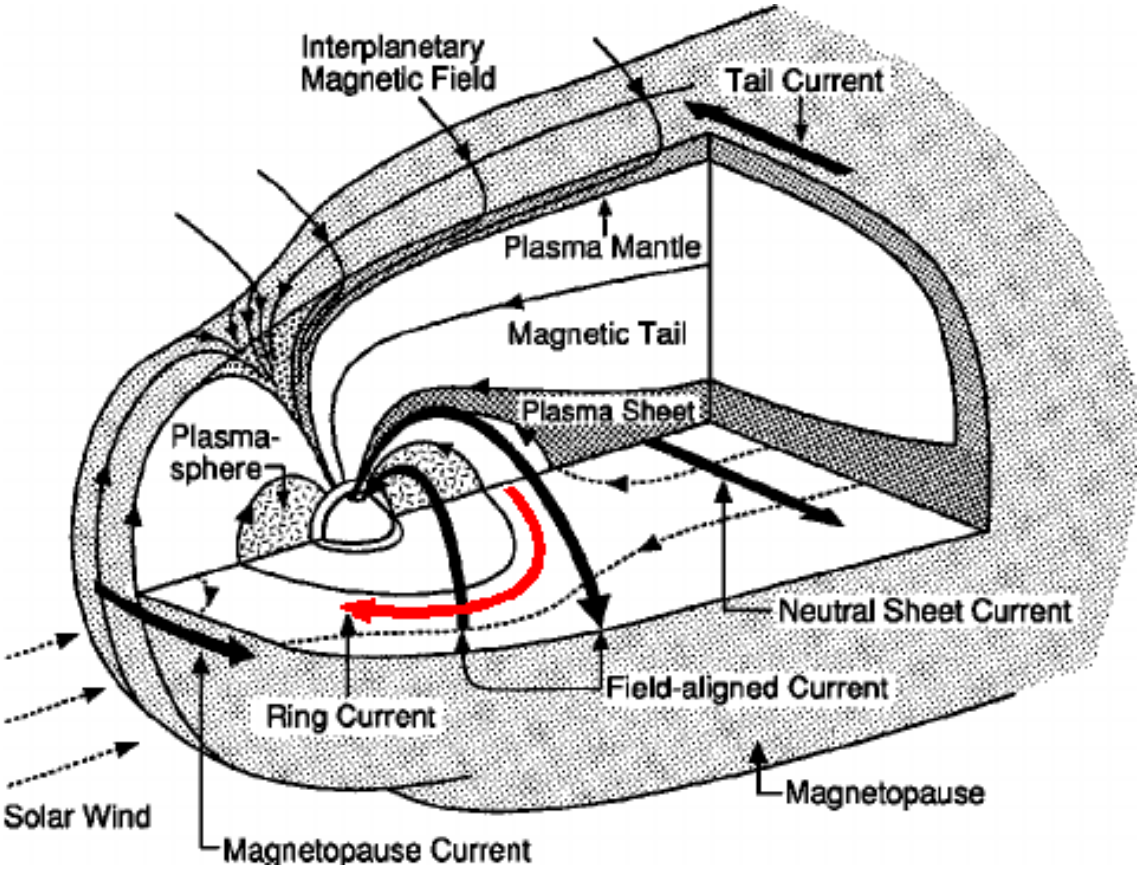

Figure 10: The terrestrial magnetosphere. Thick arrows portray electric currents with the ion component of ring current highlighted in red. Thin, solid lines correspond to magnetic field lines. Image adapted from [1].

$>$ 1.5 AU from the Sun, but whenever a CIR is formed at distances of $<$ 1 AU, they can act as drivers of geomagnetic storms. A CIR consists of a region of compressed and accelerated slow solar wind followed by a region of compressed and slowed fast solar wind. Between these is a discontinuity separating the two streams and in some cases, the CIR includes leading and trailing shocks. The shape of the CIR follows the rotation and spiral-like form of the solar magnetic field. The magnetic flux density of the solar magnetic field is increased within the CIR [62].

Evolution of geomagnetic storms can be partitioned into three phases. The mechanisms related to these phases differ based on the cause of the storm. Here only CIR-driven storms are considered. The "initial phase" is recognisable from a rise

in the Dst index. The CIR compresses the magnetosphere when it first comes into contact with it, causing the magnetic flux density of the terrestrial magnetic field and magnetopause current to increase. In the "main phase" magnetic reconnection and transfer of solar wind particles inject energy into the magnetosphere, and the resulting changes in magnetospheric current systems lead to a decreasing Dst index. In CIR-driven storms the Dst index rarely falls below -100 nT, because the component of the interplanetary magnetic field antiparallel to the terrestrial magnetic field is relatively unstable in time. Finally, in the "recovery phase", the Dst index returns to values typical of a quiet magnetosphere and the ring current decays. [63]

In Fig. 11 the upper panel shows the progress of the storm. The main difference between the SYM-H and Dst indexes in this context is that the former has better time resolution [64]. The weakening of the magnetic field related to the main phase starts at 2:00 UT and ends at 6:00 UT. While the relatively slow recovery phase starts at 6:00 UT, there is a second dip in SYM-H between 8:00 UT and 9:15 UT. This is caused by the interplanetary magnetic field changing direction one more time [4].

While the storm was imaged stereoscopically for a fraction of its duration, the other benefit of having two instruments was that detections from TWINS-2 could be used to cover time intervals during which TWINS-1 was unavailable. The ENA maps of Fig. 11 are results of integrating over 30 minutes, with integration starting at the times indicated in the figure. Here O and H ENAs have been statistically separated based on distributions of "start"-pulse heights. [4]

In most of the ENA images, the hottest pixels can be found near the auroral zone of Earth. These are caused by Low Altitude Emission (LAE) consisting of ions that have precipitated into the atmosphere of Earth and undergone several charge exchanges before escaping. Because of the Molniya orbits the TWINS-spacecraft had, they could produce coverage of emissions like these for longer timescales and

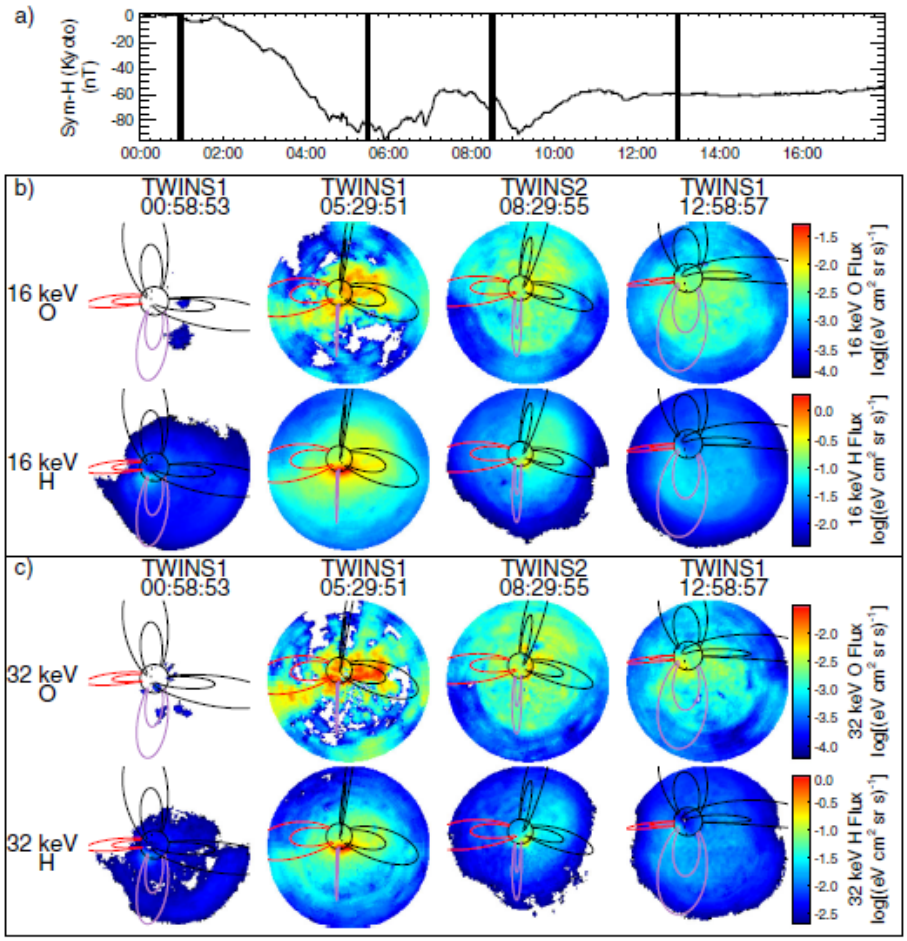

Figure 11: The 22 July 2009 storm. a): SYM-H index as a function of time, b): H and O ENA detections at 16 keV, c): Same for 32 keV. Magnetic field lines are for $L = 4$ and $L = 8$, while red lines are in the noon direction and purple lines in dusk direction. Image taken from [4].

for larger variations of MLT than singular ENA instruments or *in situ*-probes. This has made it possible to extract information about the precipitating ions from ENA data [65].

In both energies of Fig. 11 the oxygen emission is fainter than that of hydrogen, which reflects the relative abundances of these elements. During storms, the relative abundance of O is enhanced, and in very severe storms it can even surpass that of hydrogen [59]. It can be noted that oxygen emission decays much slower than that

of hydrogen. This is because charge exchange is a significant mechanism of ring current decay and at energies < 50 keV the charge exchange rate of O is lower than that of H [59]. In Fig. 11 the decay of O also seems faster in the channel of lower energy.

Fig. 12 presents four convolved images, two from the main phase of the 22 July 2009 storm and two from the recovery phase. These data represent only hydrogen fluxes integrated over pitch angles. Because the color scales for each image are different, these images are included because they show how ENA observations can be used to study the asymmetry of the ring current and its changes during the storm. The subfigures labelled 0544 UT and 0844 UT coincide temporally with the two central rows of ENA images in Fig. 11. Since the energy channel used in Fig. 12 is 15 ± 7.5 keV, the fluxes in the images coincide best with the 16 keV energy channel in Fig. 11 [66]. The method of convolution used is similar to the parametrised model introduced in 2.6.3 [66]. Since the goal has been to estimate 2D distribution of ion fluxes, it has not been possible to include the LAE regions near Earth in the inversions.

From Fig. 12 it can be seen that the asymmetry is at its greatest in the main phase of the storm while SYM/H is still falling. The asymmetry is significantly lessened at the image labelled 1114 UT, which shows the ring current during the recovery phase. While this progression can be tied to changes ASY/H index, which measures the asymmetric horizontal component of the magnetic field [66], it has also been estimated that most of the partial ring current in the dusk side would have been closed in the ionosphere during the main phase [67].

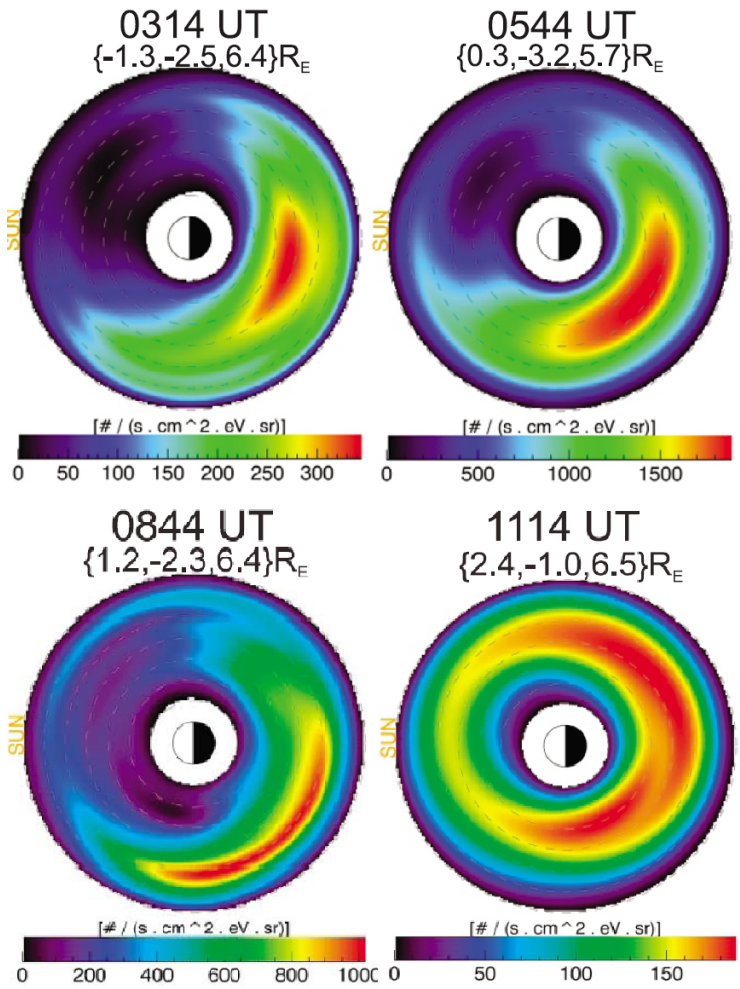

Figure 12: The 22 July 2009 storm in ion fluxes convolved from hydrogen ENA data. The upper images are from TWINS 1 while the lower ones are from TWINS 2. The energy range is 7.5-22.5 keV and integration time is the given UT $\pm$15 min. Note that the colors related to ion fluxes are different for all images. Images taken from [66].

4 Terrestrial ring current as a foreground: Observations of solar ENAs from Low Earth Orbit

As mentioned in chapter 1, it is possible that ENAs can result from charge exchanges between H^+ and heavier ions within the solar atmosphere. These ENAs could in theory then be detectable even at Low Earth Orbit (LEO), since they could penetrate the region where the terrestrial magnetosphere can redirect charged particles. On the other hand, this is also a case where the terrestrial ring current acts as a source of ENA background, which must be accounted for. In this chapter, the feasibility of a very high energy ENA detector in LEO is examined by estimating signal to noise ratios at different energy intervals during a geomagnetic storm. In order to do this, two cases of ENA flux measurements were used to estimate the spectra of solar ENAs and storm time ring current ENAs, respectively. These, in turn, were used to estimate relative count rates for the detector, which was yet to be built at the time this work was written.

In the context of solar ENA measurements the signal consists of solar ENA counts detected in addition to the ENA background counts of the terrestrial magnetosphere. The resulting time-averaged counts are assumed to contain Poisson-distributed noise. The goal of this chapter is to examine whether the additional solar ENA counts can be distinguishable from the variations that can be attributed to the noise during a geomagnetic storm.

4.1 The motivation for looking for solar ENAs

Currently, there is only one known case of possible solar ENA detection, the one mentioned in [7] and depicted in Fig. 13. The detectors used were the Low Energy Telescopes (LET) aboard STEREO A and B spacecraft, which were at the time relatively close to each other and Earth. LETs aren't capable of discriminating

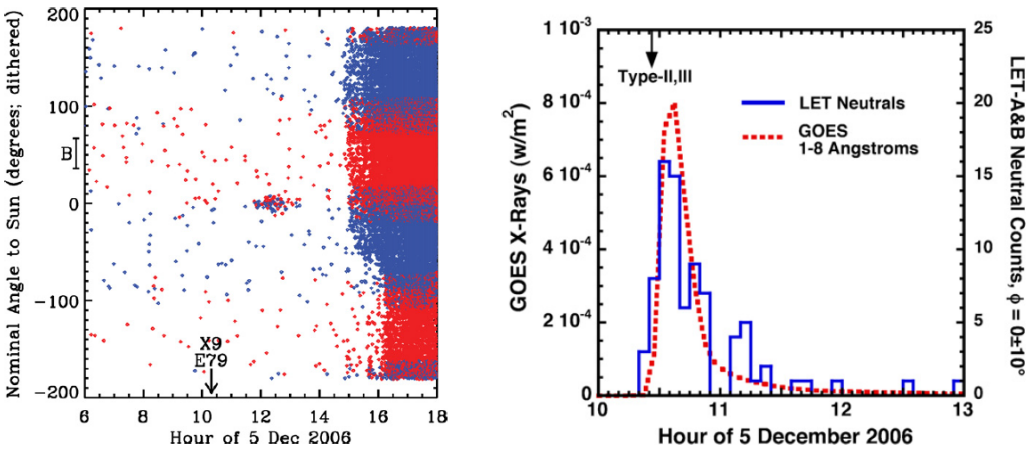

(a) (b)

Figure 13: The detection of 5.12.2006. In (a) the angle of arrival is a function of time, red is for particles detected with LET-A and blue for detections with LET-B. The bracket "B" refers to the directions at which the solar magnetic field lines point towards the terrestrial magnetosphere, and "X9" marks the onset of the flare. In (b) 5-minute counts of particles from the direction of Sun are in blue and corresponding X-ray emission in red. The arrival times of neutrals have been shifted to allow comparison with the X-ray profile. Both images are taken from [7].

between charged and neutral particles, but the timing, direction of propagation and emission profile can all be used to argue that the detected particles were ENAs from the Sun.

In panel (a) of Fig. 13 the possible ENAs arrive approximately 2 hours before the main Solar Energetic Particle (SEP) event. The direction of arrival is $\pm 10°$ of the Sun, and well off from the range of angles at which the interplanetary magnetic field points towards Earth. These characteristics can be the result of ENAs originating near a solar eruption and travelling away from it in straight lines. On the other hand, in panel (b) of Fig. 13 the time-shifted emission profile of neutrals is similar to that of X-rays detected during the solar event. This suggests that they have the same source. [7]

The lack of corroborating observations may be explained by the fact that there has never been a dedicated high energy ENA detector specifically built for observation of the Sun. Because of this, other solar ENA spikes may have been indistinguishable from the backgrounds of SEPs [68]. Using the terrestrial magnetosphere to naturally filter out the solar wind and observing at energy ranges higher than those at which ring current flux is at its highest allow testing of the solar ENA hypothesis.

Observations of solar ENAs would also give new insights to SEPs, especially at sub-MeV energies [69]. Replenishment of particles in the corona via charge exchanges and ionisations could also be studied [70].

4.2 Particle telescope

The PArticle TElescope (PATE) is designed to take up 1.5 units of a 3-unit CubeSat. Two detectors of the type shown in Fig. 14 will be installed, one looking into the Sun and parallel with the axis of spin of the satellite, while the other is mounted in a perpendicular direction. The task of the perpendicular detector is to scan the sky for energetic particles in an effort to measure the background flux, which might interfere with the solar ENA measurements. The detector has three SSDs between two anti-coincidence detectors. A foil is used to filter out UV photons and oxygen.

4.3 Estimation of solar ENA spectrum

In [7] it was estimated that the spectrum of the solar ENA injection would have been of shape $E^{-2.46}$, and that the spectrum would have crossed a point for which the ENA flux would have been 10 $\frac{1}{(\mathrm{cm}^2 \cdot \mathrm{MeV})}$ at $E = 2\,\mathrm{MeV}$. The duration of the injection was estimated to be 90 min.

Based on this, it was possible to estimate the flux of ENAs from the Sun $F_\odot$,

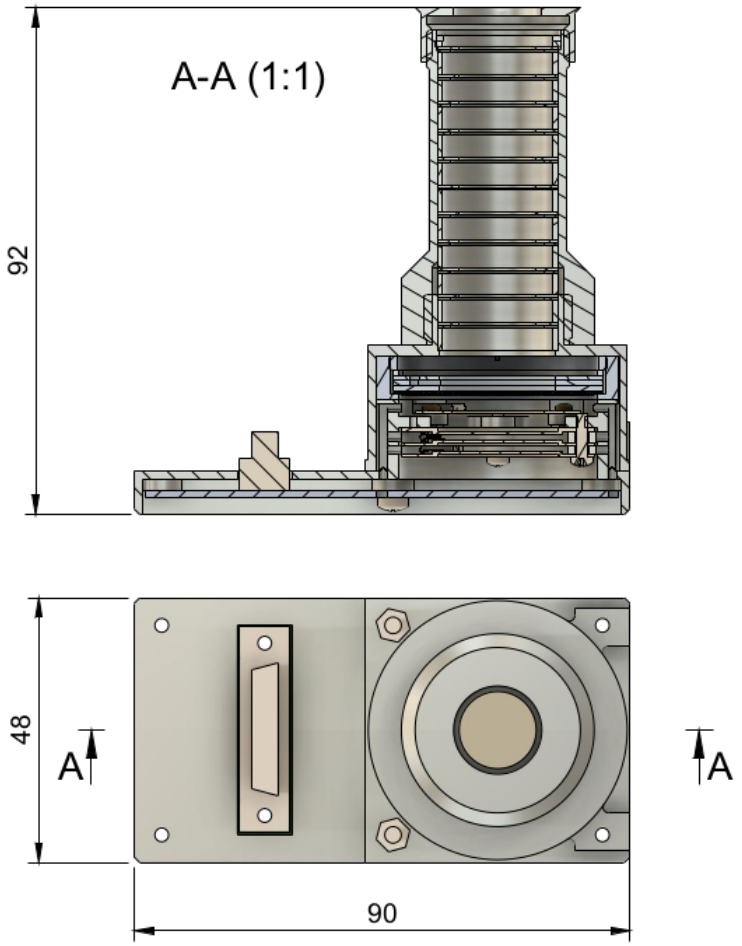

Figure 14: The PATE instrument for detecting solar ENAs. The measurements are in millimetres. Figure courtesy of Pasi Virtanen.

which had the form

$$F_{\odot} = b \cdot E[\mathrm{keV}]^{-2.46}.$$

The values estimated for flux and energy were plugged into the above equation so that the constant coefficient b could be solved:

$$b\,(2000)^{-2.46} = \frac{10}{\mathrm{cm}^2 \cdot 1000\,\mathrm{keV}},$$

$$b = \frac{0.01 \cdot 2000^{2.46}}{\mathrm{cm}^2 \cdot\ \mathrm{keV}} = 1.32 \cdot 10^6 \frac{1}{\mathrm{cm}^2 \cdot\ \mathrm{keV}},$$

$$F_{\odot} = 1.32 \cdot 10^6 \frac{1}{\mathrm{cm}^2 \cdot \mathrm{keV}} \cdot E[\mathrm{keV}]^{-2.46}.$$

In order to calculate the signal to noise ratios, the number of detections during 45 min = 2700 s into a detector with an area of 2 cm^2 had to be estimated. In this examination, it was assumed that all of the solar ENA counts could be gathered during a period of 45 minutes. Since the FoV of PATE will cover the entire solar disk, the geometric factor of the instrument wasn't considered when calculating counts of solar ENAs. Because of these considerations, the amounts of detections within 45 min to an area of 2 cm^2 were computed from

$$S = 2\,\mathrm{cm}^2 \cdot 1.32 \cdot 10^6 \frac{1}{\mathrm{cm}^2 \cdot \mathrm{keV}} \cdot \int_{E_1}^{E_2} E[\mathrm{keV}]^{-2.46}\,\mathrm{d}E, \tag{19}$$

where E_1 and E_2 were the limits of the energy channel in use. It should be noted that the actual spike in solar ENA flux can be wider or narrower than the 45 minute observation time, or its peak can be situated outside of the time window during which PATE has a clear view of the Sun. While the scenario corresponding to Eq. (19) could be unrealistic, it serves as a useful point of comparison.

4.4 Estimation of storm time ring current ENA spectrum

The goal here was to estimate high energy hydrogen ENA counts during a geomagnetic storm based on figure 4 of [71], which is reproduced partially in this work as Fig. 15. The averaged neutral hydrogen fluxes for areas 1 and 2 shown in panels (b) and (c) of Fig. 15 were estimated from the integrated fluxes in the figures, and based on this, corresponding differential fluxes were calculated for the three energy channels. Two different functions were fitted to these spectra, and fitting results were used to extrapolate the fluxes at even higher energies. A preliminary value of the geometric factor of PATE was used to estimate the counts caused by the ring current. These were then compared with corresponding counts obtained with Eq.

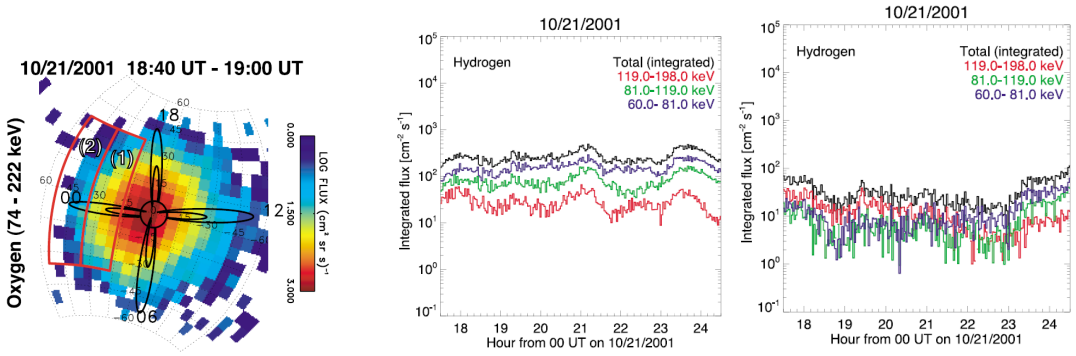

(a) (b) (c)

Figure 15: (a) An ENA image with the limits of areas 1 and 2, (b) integrated flux from area 1, (c) integrated flux from area 2. All images taken from [71].

(19) to produce the estimated signal to noise ratios. All fits were done in gnuplot 5.0 using the least squares method.

It can be noted that in [71] the ring current ENA fluxes are a result of observations from a vantage point nearly above the Earth's pole. In observations of the Sun from LEO, the vantage point is much closer to the equatorial plane. In the following analysis, therefore, it was assumed that the ring current ENA emission region is toroidal and that the emission is isotropic. This is a reasonable simplification because the goal is to estimate realistic upper limits for the background flux.

4.4.1 First estimation of spectrum

Energy channels used in Fig. 15 and in the calculation of differential fluxes are shown in Table 2. As a first estimate for channel average energy, geometric means of channel limits were used.

Table 2: Energy channels of HENA. All energies are in keV and channel numbering is arbitrary.

Channel	E_1	E_2	$\langle E \rangle = \sqrt{E_1 \cdot E_2}$	$\Delta E = E_2 - E_1$
1	60	81	70	21
2	81	119	98	38
3	119	198	154	79

Based on Fig. 15, fluxes integrated over areas and energy ranges ΔE were estimated and collected, along with estimated errors, to Table 3. These fluxes were estimated from panels (b) and (c) of Fig. 15, from time coordinate 24. To calculate corresponding differential fluxes, it was necessary to divide the integrated flux values with products of corresponding energy range and solid angle subtended by the area.

Each area equalled approximately the combined areas of 36 pixels. Single pixel was assumed to be 6° by 6°, or 0.10472 rad by 0.10472 rad. The limits of integration were taken from the figure. Therefore the solid angles subtended by areas 1 and 2 shown in the figure were estimated as follows:

$$\Omega = \int_0^{3 \cdot 0.10472\,\mathrm{rad}} \int_{\frac{\pi}{2}+6 \cdot 0.10472\,\mathrm{rad}}^{\frac{\pi}{2}-6 \cdot 0.10472\,\mathrm{rad}} \sin\theta \,\mathrm{d}\theta \,\mathrm{d}\varphi,$$

$$\Omega = 3 \cdot 0.10472\,\mathrm{rad} \cdot \left[\cos\left(\frac{\pi}{2} - 6 \cdot 0.10472\,\mathrm{rad}\right) - \cos\left(\frac{\pi}{2} + 6 \cdot 0.10472\,\mathrm{rad}\right)\right],$$

$$\Omega = 0.36932\,\mathrm{sr}.$$

Table 3: Integrated fluxes estimated from Fig. 15 at time = 24 and differential fluxes calculated from these.

Area	ΔE [keV]	J [1/(cm^2·s)]	$\left\langle \frac{\mathrm{d}J}{\mathrm{d}E} \right\rangle$ [1/(cm^2·s · sr · keV)]
1	21	210 ± 10	27 ± 2
1	38	110 ± 10	7.8 ± 0.8
1	79	22 ± 5	0.8 ± 0.2
2	21	35 ± 5	4.5 ± 0.7
2	38	20 ± 3	1.4 ± 0.3
2	79	8 ± 3	0.3 ± 0.1

Calculation example: Line two of Table 3:

$$\left\langle \frac{\mathrm{d}J}{\mathrm{d}E} \right\rangle = 110 \frac{1}{(\mathrm{cm}^2 \cdot \mathrm{s})} \cdot \frac{1}{38\,\mathrm{keV} \cdot 0.36932\,\mathrm{sr}} \pm 10 \frac{1}{(\mathrm{cm}^2 \cdot \mathrm{s})} \cdot \frac{1}{38\,\mathrm{keV} \cdot 0.36932\,\mathrm{sr}},$$

$$\left\langle \frac{\mathrm{d}J}{\mathrm{d}E} \right\rangle \approx (7.8 \pm 0.8) \frac{1}{(\mathrm{cm}^2 \cdot \mathrm{s} \cdot \mathrm{sr} \cdot \mathrm{keV})}.$$

Two different functions were fitted to the two sets of data in Table 3. The results were collected to Tables 4 and 5.

Table 4: Results of fitting a function of form $\frac{\mathrm{d}J}{\mathrm{d}E} = b \cdot e^{aE}$.

Area	a [keV^{-1}]	b [1/(cm^2·s · sr · keV)]
1	-0.0442 ± 0.0007 (1.5%)	590 ± 30 (4.8%)
2	-0.040 ± 0.004 (9.6%)	76 ± 22 (28.5%)

Table 5: Results of fitting a function of form $\frac{\mathrm{d}J}{\mathrm{d}E} = b \cdot E^a$.

Area	a [keV^{-1}]	b [1/(cm^2·s · sr · keV)]
1	-3.8 ± 0.3 (6.2%)	$2.6{\cdot}10^8 \pm 2.6{\cdot}10^8$ (99.6%)
2	-3.46 ± 0.02 (0.4%)	$1.10{\cdot}10^7 \pm 0.07{\cdot}10^7$ (6.4%)

Based on images produced with gnuplot and errors of fit, the best two cases were selected. Based on the first line of Table 4

$$\left\langle \frac{\mathrm{d}J}{\mathrm{d}E} \right\rangle = 590 \cdot e^{-0.0442 \cdot E[\mathrm{keV}]} \frac{1}{(\mathrm{cm}^2 \cdot \mathrm{s} \cdot \mathrm{sr} \cdot \mathrm{keV})}, \tag{20}$$

and based on the second line of Table 5

$$\left\langle \frac{\mathrm{d}J}{\mathrm{d}E} \right\rangle = 1.10 \cdot 10^7 \cdot E[\mathrm{keV}]^{-3.46} \frac{1}{(\mathrm{cm}^2 \cdot \mathrm{s} \cdot \mathrm{sr} \cdot \mathrm{keV})}. \tag{21}$$

4.4.2 Iterative corrections to average energies

More accurate values of the channel mean energies were determined by iteration. First, the average energy was defined as

$$\langle E \rangle = \frac{\int_{E_1}^{E_2} E \frac{\mathrm{d}J}{\mathrm{d}E} \mathrm{d}E}{\int_{E_1}^{E_2} \frac{\mathrm{d}J}{\mathrm{d}E} \mathrm{d}E}, \tag{22}$$

where E_1 and E_2 were the same as in Table 2 and $\frac{\mathrm{d}J}{\mathrm{d}E}$ was taken from the previous results of fitting.

Next, the fitting of the exponential function to area 1 was used. The integral (22), solved and rearranged for plugging in the constants obtained from the fit of the exponential function, was as follows:

$$\langle E \rangle_{exp} = \frac{\left[e^{aE_2} (aE_2 - 1) - e^{aE_1} (aE_1 - 1) \right]}{a \left(e^{aE_2} - e^{aE_1} \right)}. \tag{23}$$

The only parameter changed between iterations was the value of a obtained from fits. After new average channel energies were calculated from Eq. (23), they were used with differential fluxes from Table 3 to perform a fit of an exponential function. From the fit, the next value for a was obtained.

The iterations were continued until the difference between consecutive values of a were unchanged to the fourth decimal place, at which point the difference between

consecutive values of $\langle E \rangle$ was less than 1 keV. Four iterations were needed for this.

The iteration was also done for the case of $\frac{\mathrm{d}J}{\mathrm{d}E} \propto E^a$. Now the function into which the values of a were input was

$$\langle E \rangle_{pow} = \frac{(a+1)}{(a+2)} \cdot \frac{\left[E_2^{(a+2)} - E_1^{(a+2)}\right]}{\left[E_2^{(a+1)} - E_1^{(a+1)}\right]}. \tag{24}$$

Here data from area 2 was used, so the first value of the fitting parameter was taken from the second line of Table 5: $a = -3.46$. After 3 iterations the values of energy exhibited changes of less than 0.1 keV between iterations. The end results are shown in Table 6.

Table 6: The average energies obtained with iteration for exponential and power-law spectra. All energies are in keV.

Chnl.	E_1	E_2	$\langle E \rangle_{exp}$	$\langle E \rangle_{pow}$	$0.5 \cdot (\langle E \rangle_{exp} + \langle E \rangle_{pow})$
1	60	81	69	69	69
2	81	119	94	96	95
3	119	198	138	147	143

In the above table, the energies of channels 1 and 2 are almost unaffected by the choice of the function while in the case of channel 3 the difference is 9 keV. Therefore the value of 138 keV could be seen as an estimated lower limit. From Fig. 16 it can be seen that even with channel 3 energy of 147 keV the exponential spectrum would be the one that corresponds better to the differential fluxes measured from area 1. The average channel energies used in the rightmost column are used in the calculations that follow.

4.4.3 Spectrum estimation with iterated energies

The fitting of functions of forms $\frac{\mathrm{d}J}{\mathrm{d}E} = b \cdot e^{aE}$ and $\frac{\mathrm{d}J}{\mathrm{d}E} = b \cdot E^a$ to differential fluxes in Table 3 was done again, but now the average energies were taken from the rightmost

column of Table 6. The results of fitting are seen in Figures 16 and 17 and Tables 7 and 8.

Table 7: Results of fitting a function of form $\frac{\mathrm{d}J}{\mathrm{d}E} = b \cdot e^{aE}$.

Area	a [keV^{-1}]	b [1/(cm^2·s · sr · keV)]
1	-0.0477 ± $6 \cdot 10^{-5}$ (0.1%)	728 ± 3 (0.4%)
2	-0.044 ± 0.004 (7.4%)	90 ± 30 (23.3%)

Table 8: Results of fitting a function of form $\frac{\mathrm{d}J}{\mathrm{d}E} = b \cdot E^{a}$.

Area	a [keV^{-1}]	b [1/(cm^2·s · sr · keV)]
1	-4.0 ± 0.3 (7.2%)	$6{\cdot}10^8$ ± $8{\cdot}10^8$ (122.5%)
2	-3.67 ± 0.03 (0.7%)	$2.5{\cdot}10^7$ ± $0.3{\cdot}10^7$ (11.6%)

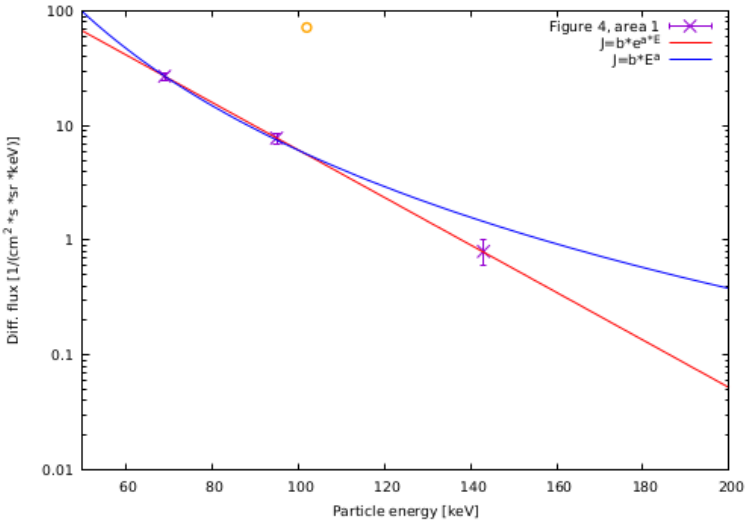

Figure 16: Spectrum corresponding to area 1 according to Table 3. The energies are now taken from Table 6. The circle represents flux from a hot pixel.

Based on images and errors of fit, the best two cases were selected. Based on the first line of Table 7

$$\left\langle \frac{\mathrm{d}J}{\mathrm{d}E} \right\rangle_{exp} = 728 \cdot e^{-0.0477 \cdot E[\mathrm{keV}]} \frac{1}{(\mathrm{cm}^2 \cdot \mathrm{s} \cdot \mathrm{sr} \cdot \mathrm{keV})}, \tag{25}$$

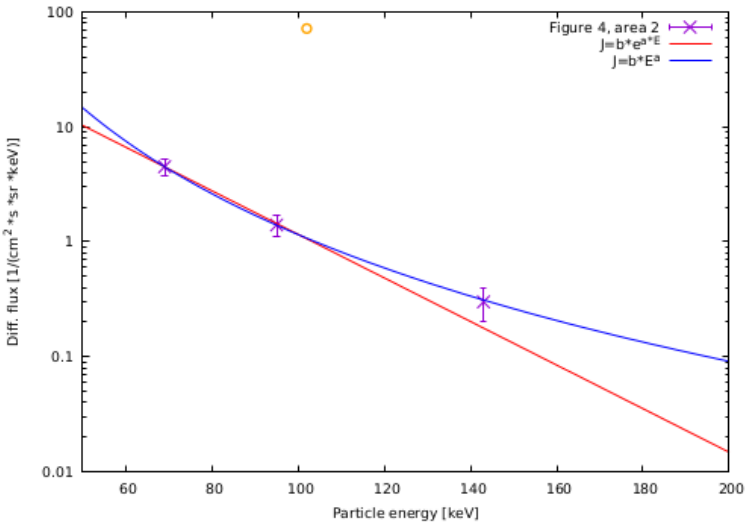

Figure 17: Spectrum corresponding to area 2 according to Table 3. The energies are now taken from Table 6. The circle represents flux from a hot pixel.

and based on the second line of Table 8:

$$\left\langle \frac{\mathrm{d}J}{\mathrm{d}E} \right\rangle_{pow} = 2.5 \cdot 10^7 \cdot E[\mathrm{keV}]^{-3.67} \frac{1}{(\mathrm{cm}^2 \cdot \mathrm{s} \cdot \mathrm{sr} \cdot \mathrm{keV})}. \tag{26}$$

4.4.4 Analysis based on a single hot pixel

In Figure 3 of [71], middle row, several pixels can be seen with flux values of $10^4 \frac{1}{(\mathrm{cm}^2 \cdot \mathrm{s} \cdot \mathrm{sr})}$ with energy range 60-198 keV. One of the images of this row is shown as Fig. 18 of this document. These hot pixels were used as a yardstick for a worst case scenario of background ENA flux from the terrestrial magnetosphere. The differential flux of a hot pixel was then

$$\left\langle \frac{\mathrm{d}J}{\mathrm{d}E} \right\rangle = 10^4 \frac{1}{(\mathrm{cm}^2 \cdot \mathrm{s}\ )} \cdot \frac{1}{(198 - 60)\,\mathrm{keV} \cdot 1\,\mathrm{sr}}$$

$$\left\langle \frac{\mathrm{d}J}{\mathrm{d}E} \right\rangle \approx 72 \frac{1}{(\mathrm{cm}^2 \cdot \mathrm{s} \cdot \mathrm{sr} \cdot \mathrm{keV})}.$$

The arithmetic mean of the iterated energies in the rightmost column of Table 6 is 102 keV. Based on this, the differential flux of the hot pixel was inserted to Figures

16 and 17.

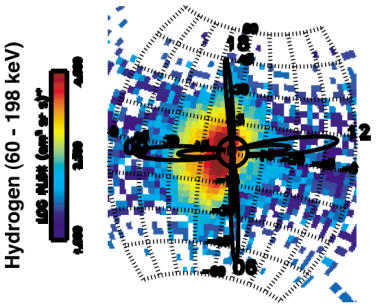

Figure 18: The ENA image used in defining the hot pixel flux. Image taken from [71].

4.5 ENA count estimation based on a single hot pixel

Both exponential and power-law spectra had to be shifted upwards to allow estimation of ENA counts corresponding to emission from a hot pixel.

In the case of the exponential spectrum a new value for the parameter b was calculated by first solving Eq. (25) for this parameter and then plugging in the values corresponding to the hot pixel:

$$\left\langle \frac{\mathrm{d}J}{\mathrm{d}E} \right\rangle_{exp} = b \cdot e^{-0.0477 \cdot E[\mathrm{keV}]},$$

$$b = 72 \frac{1}{(\mathrm{cm}^2 \cdot \mathrm{s} \cdot \mathrm{sr} \cdot \mathrm{keV})} \cdot e^{0.0477 \cdot 102},$$

$$b = 9340 \frac{1}{(\mathrm{cm}^2 \cdot \mathrm{s} \cdot \mathrm{sr} \cdot \mathrm{keV})}.$$

The count rates obtained with the exponential spectrum could now be converted to correspond to the case of up-shifted exponential spectrum by multiplying them with $\frac{9340}{728} \approx 12.83$.

The above calculation was repeated for the power-law spectrum given by Eq. (26):

$$\left\langle \frac{\mathrm{d}J}{\mathrm{d}E} \right\rangle_{pow} = b \cdot E[\mathrm{keV}]^{-3.67},$$

$$b = 72 \frac{1}{(\mathrm{cm}^2 \cdot \mathrm{s} \cdot \mathrm{sr} \cdot \mathrm{keV})} \cdot 102^{3.67},$$

$$b = 1.694 \cdot 10^9 \frac{1}{(\mathrm{cm}^2 \cdot \mathrm{s} \cdot \mathrm{sr} \cdot \mathrm{keV})},$$

$$\frac{1.694 \cdot 10^9}{2.5 \cdot 10^7} \approx 67.76.$$

4.6 Estimations of signal to noise ratios

Total ENA counts for areas 1 and 2 and for the cases of hot pixels were calculated for energy channel 3 of Table 2 and PATE energy intervals 216-300 keV, 300-420 keV and 420-580 keV. This was done by integrating the differential fluxes estimated above over the channel energies. The channel energies for PATE were determined so that $\frac{E_2}{E_1} \approx 1.39$, as a compromise between energy resolution and signal to noise ratio. The result was then multiplied with a preliminary estimate for the geometric factor of PATE $G = 0.049\,\mathrm{cm}^2 \cdot \mathrm{sr}$, and the detection time of 45 min = 2700 s.

Table 9: Detection amounts in 45 min = 2700 s in the cases of the solar ENA spectrum , exponential and power law spectra and corresponding hot pixels.

E_1	E_2	S	N_{exp}	N_{exphot}	N_{pow}	N_{powhot}
119	198	442	6750	86670	2646	179280
216	300	135	66	853	424	28620
300	420	85	1	16	179	12123
420	580	50	0.004	0.05	0.5	34

Calculation example: Fourth column on line 2 of Table 9:

$$N_{exp} = 2700\,\mathrm{s} \cdot 0.049\,\mathrm{cm^2{\cdot}sr} \cdot 728 \frac{1}{(\mathrm{cm^2{\cdot}s} \cdot \mathrm{sr} \cdot \mathrm{keV})} \int_{216\,\mathrm{keV}}^{300\,\mathrm{keV}} e^{-0.0477 \cdot E}\,\mathrm{d}E,$$

$$N_{exp} \approx 66.$$

Since the peak caused by solar ENAs must be distinguishable from fluctuations in the background of ring current ENAs, and said fluctuations are assumed to be Poisson-distributed, the signal to noise ratio can be defined as the ENA count during 45 min divided by the square root of the background count during 45 minutes.

Table 10: Signal to noise ratios calculated from values of background and signal shown in Table 9.

E_1	E_2	S	$\frac{S}{\sqrt{N_{exp}}}$	$\frac{S}{\sqrt{N_{exphot}}}$	$\frac{S}{\sqrt{N_{pow}}}$	$\frac{S}{\sqrt{N_{powhot}}}$
119	198	442	5.4	1.5	8.6	1.0
216	300	135	16.6	4.6	6.6	0.8
300	420	85	85	21.3	6.4	0.8
420	580	50	>50	>50	>50	8.6

A small Python 3 script was written to give some idea about the way an ENA flux from Sun might appear in cases of various S/N ratios. For the sake of repeatability, the listing of this script is included as an Appendix of this thesis. The results of a run of this script are seen in Figure 19. The ring current background count was assumed to be constant in time except for Poisson-distributed noise. The background values were selected so that the various S/N ratios could be showcased.

The solar ENA peak was defined in the script as

$$S = A_{height} \cdot \exp\left(-\frac{\tau_{rise}}{t - t_0} - \frac{t - t_0}{\tau_{fall}}\right)$$

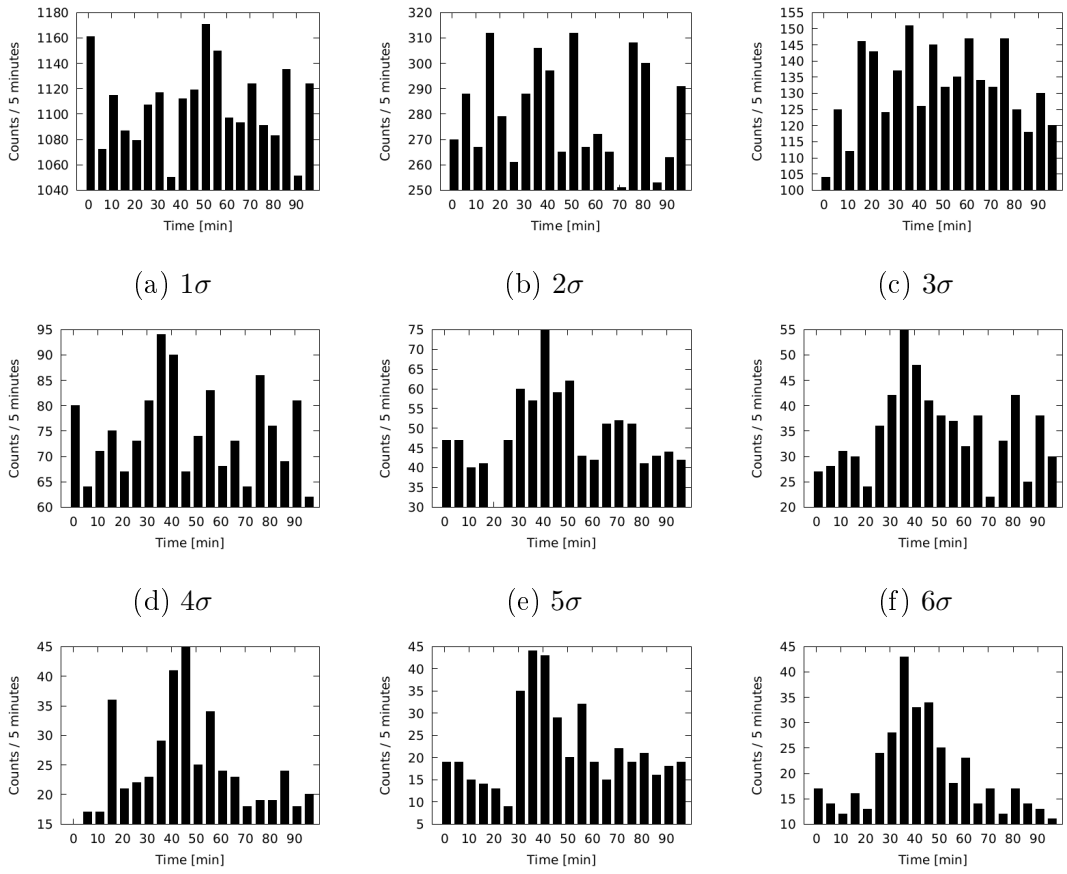

(a) 1σ (b) 2σ (c) 3σ

(d) 4σ (e) 5σ (f) 6σ

(g) 7σ (h) 8σ (i) 9σ

Figure 19: Results of computation corresponding to S = 100 with background levels varied so that cases with different S/N ratios could be examined. Notice that while the time axis in minutes is the same in each image, the ranges of y-axes vary from each other. In all figures the ENA peak starts at 25 min.

Here A_{height} is a scaling factor with such a value that the peak histogram heights, without background or Poisson-distributed fluctuations, total approximately 100. Coefficients τ_{rise} and τ_{fall} were adjusted by experimentation so that the unperturbed shape of the peak would be similar to the ENA peak shape seen in [7]. Finally, the value of t_0 was adjusted so that the peak would begin at $t = 25$ min. All columns of the resulting histograms had Poisson-distributed noise added to them.

Based on Figure 19, the ENA peak becomes distinguishable from noisy background when S/N = 5σ. In Table 10 11 cases of 16 fulfill this condition. The shape of the ENA peak is fairly well presented at S/N = 9σ, which is achieved or surpassed in 6 of the 16 cases.

4.7 Comparison with an alternative spectrum of ring current ENA emission

Since ring current ENA fluxes of over 200 keV are usually very faint, they do not provide good opportunities for observation, and thus data at these higher energies is scarce. However, for the storm of October 29-30, 1994 there is data from the EPIC instrument of the Geotail satellite, where approximate neutral hydrogen fluxes were measured to be $10^{-2}\frac{1}{(\mathrm{cm}^2 \cdot \mathrm{s} \cdot \mathrm{keV})}$ at 180keV and $10^{-3}\frac{1}{(\mathrm{cm}^2 \cdot \mathrm{s} \cdot \mathrm{keV})}$ at 270keV [72].

If these two data points were assumed to form a line in a log-log graph, the equation of this line would be

$$F(E) = D \cdot E^m,$$

for which

$$m = \frac{\log\left(\frac{F_1}{F_2}\right)}{\log\left(\frac{E_1}{E_2}\right)} = \frac{\log\left(\frac{10^{-2}}{10^{-3}}\right)}{\log\left(\frac{180}{270}\right)} \approx -5.6789$$

and

$$D = F(E_1) \cdot E_1^{-(-5.6789)} \approx 6.419 \cdot 10^{10}. \quad (27)$$

The total solid angle that the two Ion Composition System -telescopes of EPIC open into was estimated to be 0.4 sr. The ENA spectrum then became

$$\left\langle \frac{\mathrm{d}J_{Geotail}}{\mathrm{d}E} \right\rangle = 6.42 \cdot 10^{10} \cdot E[\mathrm{keV}]^{-5.68} \frac{1}{(\mathrm{cm}^2 \cdot \mathrm{s} \cdot \mathrm{keV} \cdot 0.4 \text{ sr})}. \quad (28)$$

The background count rates and S/N values corresponding to Geotail measurements were calculated as those in Table 9, and they are collected to Table 11. It can be seen that they are comparable to the relatively mild case of counts calculated with the exponential spectrum.

Table 11: Count rates calculated by integrating eq. (28) and signal to noise ratios.

E_1	E_2	S	$N_{Geotail}$	$\frac{S}{\sqrt{N_{Geotail}}}$
119	198	442	795	16
216	300	135	43	21
300	420	85	10	27
420	580	50	3	29

4.8 Conclusions

It is commonly accepted that the ring current ENA emission at energies over 200 keV is very faint, so much so that ENAs above this energy are usually not seen. The exponential spectrum based on [71] seems to be a decent yardstick for conditions of higher ring current fluxes: At energies below 200 keV the background may dominate, but at energies above 200 keV the signal to noise ratios can be excellent. The real limiting factor is, therefore, the time the instrument is exposed to Sun during an orbit. A single instrument may miss solar ENA events by being on the night side of

the Earth when they happen. A swarm of three or more spacecraft with the same orbital periods but equally distanced from their neighbours would have a higher chance of success.

5 Conclusion and outlook

ENA-related characteristics like energy-dependent charge exchange cross sections, possible loss mechanisms and effects of gravity and radiation pressure must be taken into account when interpreting ENA images. The characteristics of used instruments, together with the availability of contextual information, pose limitations to quantity and types of useful data that can be obtained, especially in the case of image inversion.

Despite these limitations and complications, ENA imaging has proven its value. Phenomena like the IBEX ribbon and anisotropies in the ring current would be difficult and expensive to study globally with only *in situ*-observations. ENA observations may also allow the study of solar eruptions from a new perspective by utilisation of relatively simple and inexpensive spacecraft.

Observations of TWINS have shown the value of imaging the same phenomenon from different vantage points. On the other hand, *in situ*-observations provide useful data for image inversion, while ENA images provide useful context for local observations. In the case of the terrestrial magnetosphere, the future of the technique might lie in the simultaneous employment of multiple ENA imaging instruments together with probes that can provide information about the magnetic field and plasma characteristics related to different current systems. IBEX has temporal gaps in its coverage, caused by the terrestrial magnetosphere, and PATE will spend a large amount of its lifetime in the shadow of Earth. Experience from TWINS shows that it is reasonable to use several spacecraft instead of one to ascertain continuous coverage.

Future developments of the technique concentrate on improving instrument characteristics. This is well exemplified by the recent approval of the Interstellar Mapping and Acceleration Probe (IMAP) by NASA [73]. This probe has scientific goals that partially overlap those of IBEX, but it will carry improved instruments with

better angular resolution and sensitivity [74].

ENAs are a good example of the way our understanding increases when a new point of view is taken into use. Solar flares, the heliosheath and magnetospheric plasma populations all have shown new features when studied with ENAs. On the other hand, it cannot be said that ENA detections alone give sufficient answers or that more traditional observation methods exist merely to give context to ENA detections. Rather the global ENA observations offer only some, but important, pieces of a greater puzzle. As technical solutions allow improved sensitivities and angular resolutions of ENA detectors, the importance and number of these pieces grows.

References

[1] M. Gruntman, Review of Scientific Instruments **68**, 3617 (1997).

[2] H.-J. Fahr, H. Fichtner and K. Scherer, Reviews of Geophysics **45**, RG4003 (2007).

[3] E. J. Zirnstein *et al.*, The Astrophysical Journal **783**, 129 (2014).

[4] P. W. Valek *et al.*, Journal of Geophysical Research (Space Physics) **118**, 3377 (2013).

[5] H. Lammer and S. J. Bauer, Planetary and Space Science **41**, 657 (1993).

[6] S. Orsini *et al.*, Planetary and Space Science **58**, 166 (2010).

[7] R. A. Mewaldt *et al.*, The Astrophysical Journal Letters **693**, L11 (2009).

[8] B. G. Lindsay and R. F. Stebbings, Journal of Geophysical Research (Space Physics) **110**, A12213 (2005).

[9] M. Bzowski *et al.*, Astronomy and Astrophysics **491**, 7 (2008).

[10] P. Garnier *et al.*, Journal of Geophysical Research (Space Physics) **113**, A10216 (2008).

[11] P. Swaczyna *et al.*, The Astrophysical Journal **823**, 119 (2016).

[12] M. Bzowski, Astronomy and Astrophysics **488**, 1057 (2008).

[13] L. I. Shestakova, Solar System Research **49**, 139 (2015).

[14] H. Kucharek *et al.*, The Astrophysical Journal Supplement Series **220**, 35 (2015).

[15] A. Vorburger *et al.*, Journal of Geophysical Research (Space Physics) **119**, 709 (2014).

[16] E. Kirsch, S. M. Krimigis, W.-H. Ip and G. Gloeckler, Nature **292**, 718 (1981).

[17] S. Barabash *et al.*, Washington DC American Geophysical Union Geophysical Monograph Series **103**, 257 (1998).

[18] S. Barabash, IFR Scientific Report **228**, (1995).

[19] NASA [online, referenced 25.10.2018]. Available in www-form https://solarsystem.nasa.gov/missions/cassini/overview/.

[20] S. M. Krimigis *et al.*, Space Science Reviews **114**, 233 (2004).

[21] eoPortal [online, referenced 25.7.2018]. Available in www-form https://directory.eoportal.org/web/eoportal/satellite-missions/i/image-mission.

[22] D. G. Mitchell *et al.*, Space Science Reviews **91**, 67 (2000).

[23] C. J. Pollock *et al.*, Space Science Reviews **91**, 113 (2000).

[24] S. McKenna-Lawlor *et al.*, Annales Geophysicae **23**, 2825 (2005).

[25] eoPortal [online, referenced 15.10.2018]. Available in www-form https://directory.eoportal.org/web/eoportal/satellite-missions/t/twins.

[26] D. J. McComas *et al.*, Space Science Reviews **142**, 157 (2009).

[27] D. J. McComas *et al.*, The Astrophysical Journal Supplement Series **229**, 41 (2017).

[28] H. O. Funsten *et al.*, Space Science Reviews **146**, 75 (2009).

[29] P. C:Son Brandt *et al.*, Journal of Geophysical Research (Space Physics) **107**, 1454 (2002).

[30] S.-Y. Ma, W.-N. Yan and L. Xu, Journal of Geophysical Research (Space Physics) **120**, 9334 (2015).

[31] J. D. Perez, M. C. Fok and T. E. Moore, Space Science Reviews **91**, 421 (2000).

[32] S. Nakano *et al.*, Journal of Geophysical Research (Space Physics) **113**, A05208 (2008).

[33] J. D. Perez *et al.*, Journal of Geophysical Research (Space Physics) **109**, A05208 (2004).

[34] C. E. McIlwain, Space Science Reviews **5**, 585 (1966).

[35] C. Vallat *et al.*, Journal of Geophysical Research (Space Physics) **109**, A04213 (2004).

[36] SwRI [online, referenced 12.9.2018]. Available in www-form http://ibex.swri.edu/archive/2011.11.14.shtml.

[37] NASA [online, referenced 28.10.2018]. Available in www-form https://www.nasa.gov/mission_pages/ibex/images/index.html.

[38] D. J. McComas *et al.*, Space Science Reviews **146**, 11 (2009).

[39] Heavens Above [online, referenced 12.9.2018]. Available in www-form https://heavens-above.com/orbit.aspx?satid=33401.

[40] S. A. Fuselier *et al.*, Space Science Reviews **146**, 117 (2009).

[41] F. Allegrini *et al.*, Space Science Reviews **146**, 105 (2009).

[42] K. J. Trattner *et al.*, Journal of Geophysical Research (Space Physics) **118**, 4425 (2013).

[43] G. P. Zank, Annual Review of Astronomy and Astrophysics **53**, 449 (2015).

[44] H. Washimi, T. Tanaka and G. P. Zank, The Astrophysical Journal Letters **846**, L9 (2017).

[45] NASA [online, referenced 30.10.2018]. Available in www-form https://voyager.jpl.nasa.gov/news/details.php?article_id=110.

[46] W. Pryor *et al.*, Astronomy and Astrophysics **491**, 21 (2008).

[47] V. Izmodenov, B. E. Wood and R. Lallement, Journal of Geophysical Research (Space Physics) **107**, 1308 (2002).

[48] SwRI [online, referenced 04.11.2018]. Available in www-form http://ibex.swri.edu/archive/2012.05.10.shtml.

[49] D. J. McComas *et al.*, The Astrophysical Journal Supplement **203**, 1 (2012).

[50] D. J. McComas, W. S. Lewis and N. A. Schwadron, Reviews of Geophysics **52**, 118 (2014).

[51] V. Florinski *et al.*, The Astrophysical Journal **719**, 1097 (2010).

[52] J. Giacalone and J. R. Jokipii, The Astrophysical Journal Letters **812**, L9 (2015).

[53] SwRI [online, referenced 28.10.2018]. Available in www-form http://twins.swri.edu/BrowsePlot?mode=200.

[54] eos.org [online, referenced 15.10.2018]. Available in www-form https://eos.org/editors-vox/the-big-picture-in-geospace.

[55] H. U. Nass, J. H. Zoennchen, G. Lay and H. J. Fahr, Astrophysics and Space Sciences Transactions **2**, 27 (2006).

[56] J. H. Zoennchen, U. Nass, H. J. Fahr and J. Goldstein, Annales Geophysicae **35**, 171 (2017).

[57] SwRI [online, referenced 26.7.2018]. Available in www-form http://twins.swri.edu/mission.jsp.

[58] N. Y. Ganushkina *et al.*, Annales Geophysicae **33**, 1369 (2015).

[59] I. A. Daglis, R. M. Thorne, W. Baumjohann and S. Orsini, Reviews of Geophysics **37**, 407 (1999).

[60] S. Dubyagin, N. Ganushkina, M. Kubyshkina and M. Liemohn, Journal of Geophysical Research (Space Physics) **119**, 7243 (2014).

[61] E. Echer *et al.*, Advances in Space Research **35**, 855 (2005).

[62] I. G. Richardson, Living Reviews in Solar Physics **15**, 1 (2018).

[63] B. T. Tsurutani *et al.*, Journal of Geophysical Research (Space Physics) **111**, A07S01 (2006).

[64] J. A. Wanliss and K. M. Showalter, Journal of Geophysical Research (Space Physics) **111**, A02202 (2006).

[65] J. Goldstein and D. J. McComas, Space Science Reviews **180**, 39 (2013).

[66] J. D. Perez *et al.*, Journal of Geophysical Research (Space Physics) **117**, A09221 (2012).

[67] S. Dubyagin *et al.*, Journal of Geophysical Research (Space Physics) **118**, 5616 (2013).

[68] M. Desai and J. Giacalone, Living Reviews in Solar Physics **13**, 3 (2016).

[69] N. Vilmer, A. L. MacKinnon and G. J. Hurford, Space Science Reviews **159**, 167 (2011).

[70] H. S. Hudson, A. L. MacKinnon, M. L. De Rosa and S. F. N. Frewen, The Astrophysical Journal Letters **698**, L86 (2009).

[71] K. Keika *et al.*, Journal of Geophysical Research (Space Physics) **115**, A00I12 (2010).

[72] A. T. Y. Lui *et al.*, Advances in Space Research **20**, 351 (1997).

[73] NASA [online, referenced 20.11.2018]. Available in www-form https://www.nasa.gov/press-release/nasa-selects-mission-to-study-solar-wind-boundary-of-outer-solar-system.

[74] N. A. Schwadron *et al.*, Journal of Physics: Conference Series **767**, 012025 (2016).

Appendix: Python code used in chapter 4.6

```
#The method detectionSim Simulates detection of solar ENAs while a
    background of RC ENAs is present and resulting data has
    Poisson-distributed noise. Text files are created that can then be
    plotted in an external program like f.ex. gnuplot. Values of risetime
    and falltime were found by experimentation. The goal was to make the
    resulting peak resemble the shape seen in [Mewaldt et.al 2009]. ENA
    peak starts at #index 6 or 25 min and ends at index 15 or 70 min.

import math
import numpy as np


def detectionSim (solarcount, rclevel, fileindex):
   datafile_path = "C:\Dokumentit\ProGradu\Spectrum\Detection%s.txt" %
       fileindex
   i = 0
   j = 0
   k = 5
   risetime = 5      #Found by trial and error
   falltime = 1.9    #Found by trial and error
   tzero = 4         #Found by trial and error
   peak = [0]*20     #For storing the peak only
   s = [0]*20        #For storing noisy data

   #Non-scaled peak shape is created:
   while(k<20):
      peak[k] = math.exp(-risetime/(k-tzero) - (k-tzero)/(falltime))
      k = k + 1

   #Computation of noisy total count values:
   peaksum = math.fsum(peak) #Calculated for scaling of the peak
   while(i<20):
      s[i] = np.random.poisson(rclevel + (solarcount/peaksum)*peak[i])
      i = i + 1

   #Dump into a text file:
   f= open(datafile_path,"w+")
   for j in range(20):
      f.write('%d\n' % s[j])

   f.close()
   return;
```

```
#A loop that uses the method detectionSim to generate 9 result files, one
    for each value of background.

solar = 100  #ENA count distributed into the peak
ring = [1111, 278, 123, 69, 44, 31, 23, 17, 14] #Five minute background
    counts
l=0
while (l<9):
   index = str(l) #File number into a string
   detectionSim(solar, ring[l], index)
   l = l + 1
```